



Investigating the Effects of CoMoCrSi Powder Composition and Particle Size, and Annealing Heat Treatment on Microstructure and Mechanical and Tribological Performance of HVOF Sprayed Coatings

Murat Tolga Ertürk¹ · Süha Tirkeş² · Cemil Hakan Gür¹

Received: 7 March 2024 / Accepted: 9 May 2024
© The Author(s) 2024

Abstract

An investigation was conducted to analyze the mechanical properties, wear behavior, and microstructure of coatings formed by high-velocity oxygen fuel spraying of CoMoCrSi powders. The effects of varying Cr concentration and particle sizes before and after heat treatment at 900 °C for 4 h were studied comparatively. The increase in Cr and Mo elements in the expense of Co increased the structure's hardness before and after the heat treatment. As this increase was 10% in as-sprayed conditions, annealing raised the increase to 30%. Splat boundaries were the most vulnerable constituents against forces, creating a significant disadvantage in terms of structural integrity and affecting the overall performance. After annealing, the boundary strengths experienced a remarkable four-fold increase and cracks and fractures reduced significantly. The susceptibility of splat boundaries had a detrimental effect on room temperature wear behavior, and increased boundary densities led to a marked reduction in wear performance. Heat treatment induced improvements significantly increased the room temperature wear performance. At elevated temperature, the formation of oxide layers composed of CoMoO₄, Co₃O₄, MoO₃, and Cr₂O₃ overcame the weaknesses of the as-sprayed coating, reducing both the friction coefficient and wear losses. A reduced Co ratio led to the formation of an oxide blend with a higher concentration of Mo and Cr oxides on the surface, further improving the coating's wear behavior.

Keywords HVOF · CoCrMoSi coating · Annealing treatment · Surface integrity · Tribological behavior

1 Introduction

Considering the tribological properties, high-velocity oxy-fuel (HVOF) spraying become the preferable method because of its versatility and relatively more environmentally friendly properties than the other methods [1, 2]. HVOF introduces relatively higher spray velocities (1500–1800

m/s) and controlled flame temperatures in comparison to the other spray methods, which allows the production of denser coatings with reduced oxide contents content [3–5], lower residual stress [6], and less machining and consumable costs [7]. Additionally, the process yields a lower heat input preventing the deterioration of properties of substrate and powder materials [8] and results in a controlled and predictable tribological behavior [9].

In addition to the above-mentioned aspects, increased cooling rates of the process allow the production of cermet coatings with increased wear properties [7, 10]. But with the higher costs, lower workability, and machinability of cermets, metallic powders become an alternative coating solution [11]. Moreover, when wear and corrosion properties at high temperatures are considered, among the metallic powders, Co-based Triballoy alloys have become the commonly used option with the advantage of the formation of

✉ Murat Tolga Ertürk
etolga@metu.edu.tr

Süha Tirkeş
stirkes@metu.edu.tr

Cemil Hakan Gür
chgur@metu.edu.tr

¹ Metallurgical and Materials Engineering Department, Middle East Technical University, Ankara, Turkey

² Welding Technology and Non-destructive Testing Center, Middle East Technical University, Ankara, Turkey

the Laves phase in the coating structure during the HVOF process [12–16].

As one of the main constituents that has significant effect on the overall performance of the alloys, Laves is the intermetallic phase having $MgZn_2$ type composition which is formed generally as Co_3Mo_2Si or $CoMoSi$ in the Co-based Triballoys [14, 17–19]. With its high melting temperature and hardness values reaching 1000 HV, the Laves phase becomes significantly advantageous against wear at elevated temperatures [13, 20–22]. In cases where the alloy is applied by conventional procedures like welding or cladding, Laves phase crystallizes as dendrites in the Co matrix [13, 20, 23]. However, extremely high cooling rates of HVOF prevent crystallization of the Laves phase whereas, microcrystals are formed in each splat yielding generally an amorphous structure [7].

Having numerous benefits, based on the composition and production techniques, heat treatment condition and operating temperature, Triballoys have possibility to show substantial variation of the micro-structure and performance. In as-sprayed condition HVOF sprayed Triballoy coatings produces mainly amorphous structure with formation of Laves phase [4] and initial spraying parameters may lead to significant difference in resultant microstructure, mechanical properties and porosity concentration of the as-sprayed Triballoy coatings [7]. Consequently, in order to stabilize the coatings and increase the performance, effect of heat treatment was put to focus in many occasions. It appears unlikely that Triballoy alloys in their cast form would exhibit any improvement with heat treatment [24, 25]. However, it has been observed that amorphous coatings created through high-speed cooling methods are greatly impacted by heat treatment. Studies have shown that temperatures below 600 °C do not significantly affect the coating's structure or performance, but a range of 600 °C produces notable crystallization, increased hardness, and improved wear performance [26, 27]. In addition, annealing heat treatment at temperatures between 800 and 1000 °C results in increased crystallization, compactness, bond strength, and cross-sectional hardness of the coatings and also enhancing surface hardness, improving the wear behavior, and forming a protective oxide layer on the surface [28–31]. Furthermore, at elevated temperatures Triballoys successfully build oxide films of mainly Co and Mo type on surface which acts as protection and lubrication and increases the wear performance [3, 7, 32].

This study aims to contribute to the existing literature by comparing the microstructure, mechanical properties, and wear behavior of two commercially available Co based Triballoy powders T400 and T800 in both their as-sprayed condition and after annealing heat treatment. Study was focused on the inter-splat bonding strengths and their impact on the performance of coatings. While the influence of porosity on the structural integrity and performance of coatings has been

previously explored in the literature [33–35], the present study offers a novel viewpoint by examining the impact of splat-boundary density on the overall integrity of the coatings. This analysis is conducted by establishing a correlation between the splat-boundary density and powder particle size. Furthermore, a relatively longer annealing time was selected to introduce a stark contrast between the as-sprayed and heat-treated structure and, simultaneously, to see the effects of prolonged exposure to high temperature on the microstructure. In contrast to previous studies investigating the effects of annealing [28–31], to gain a deeper understanding of how microstructure modification affects overall performance, the oxide layer formed during heat treatment was deliberately removed before conducting mechanical and wear assessments.

2 Experimental Procedure

The commercial Triballoy T400 and T800 powders used in the study were directly purchased from Nadcap-accredited manufacturers Oerlikon Metco and Kennametal. Both powders were manufactured according to prime aviation manufacturer specifications. The elemental concentration of the alloys specified in the certificate of conformity supplied with the powders is specified in (Table 1). To investigate the differences among the powders sensitively, a third powder, TMix, a 1:1 weight mixture of T400 and T800, was also introduced into the study. The elemental concentration of TMix, with averages of T400 and T800, was also presented in Table 1. Thermo gravimetric analysis (TGA) and differential scanning calorimetry (DSC) of the powders were carried out in an open atmosphere with a heating rate of 10 °C/min between room temperature and 1000 °C. In order to observe the thermal behaviors of the coatings, as-sprayed coatings were removed from the substrate and crumbled into particles smaller than 3 mm. These particles were then subjected to DSC analysis, gradually heated from room temperature to 1300 °C at a rate of 10 °C/min. To ensure accurate results, the analysis was conducted in the presence of a protective N atmosphere, which allowed for the observation of microstructural changes while eliminating any potential effects of oxidation.

Table 1 Chemical analysis of powders (in wt%)

Element	T400	TMix	T800
C	<0.08	<0.08	<0.08
Si	2.6	3.0	3.4
Cr	8.5	13	18
Mo	29	29	29
Co	~60	~55	~50

The coatings were produced by an HVOF gun installed on an industrial robot arm on Inconel 718 coupons placed on a rotator. Before coating, no preheating was applied, and the temperature of the coupons was continuously measured by infrared scanners. Air jet coolings were used to prevent overheating of the samples during coating to ensure coupon temperatures were held under 200 °C. The surfaces were coated via H, O, and N flows, respectively 626, 184, and 239 NLPM, with a spray distance of 260 mm and a linear speed of 121 mm/s with a powder feed rate of 50 g/min. In order not to introduce a parameter originating from the thickness, coatings having 250–200 µm were produced.

After coating, some specimens were annealed at 900 °C for 4 h in a preheated furnace and cooled in air. Six types of specimens were produced in total (Table 2).

The surfaces and cross-sections of all specimens were ground to 2000 grit and then polished using 3- and 1-micron diamond suspension and colloidal silica. No etching was applied. The surface oxide films formed during annealing were removed following the same procedure to see the microstructure's direct effect on the general performance, eliminating the surface oxidation. Similarly, to ensure surface roughness does not vary among the specimens, roughness measurements were carried out in two perpendicular directions after specimen preparation. The highest allowable roughness value of $R_a=0.06\ \mu\text{m}$ was selected according to the results. Any specimens failing to remain below this value are further polished.

Phase percentages of all specimens were determined from the optical images which are taken from 5 different locations of 3 different coupons for each specimen type. Measurements were carried out using image analysis software by making color selecting the respective phases.

T400 and T800 powders, and all coupons in the as-coated (AC) and heat-treated (HT) state were analyzed by XRD using Cu-K α radiation in the 30°–90° interval with a 2°/min scan rate.

HV0.3 Vickers microhardness surveys were carried out over five randomly placed individual indentations on three different coupons of the same specimen type. After obtaining these results another survey of HV0.1 was done on one set of specimens over selectively selected 5 indentations that did not cause any surface fractures.

To draw out the general properties of splat bonding strength micro-scratch tests were carried out on three different coupons of the same specimen type, using a Rockwell-type diamond indenter with a 100 µm radius. During the tests, a scratch of

5 mm was formed by applying a load between 0.2 and 20 N with a loading rate of 19.8 N/min.

Wear performance was determined by performing pin-on-disc wear tests at room temperature and 600 °C using an Alumina pin having a 6 mm diameter. A load of 5 N with 350 m wear length and 0.1 m/s linear speed was used.

Coating surfaces, hardness indentations, and surfaces of the scratch-tested specimens were examined by a scanning electron microscope (SEM) and an optical microscope. EDX analysis was also carried out.

3 Results and Discussion

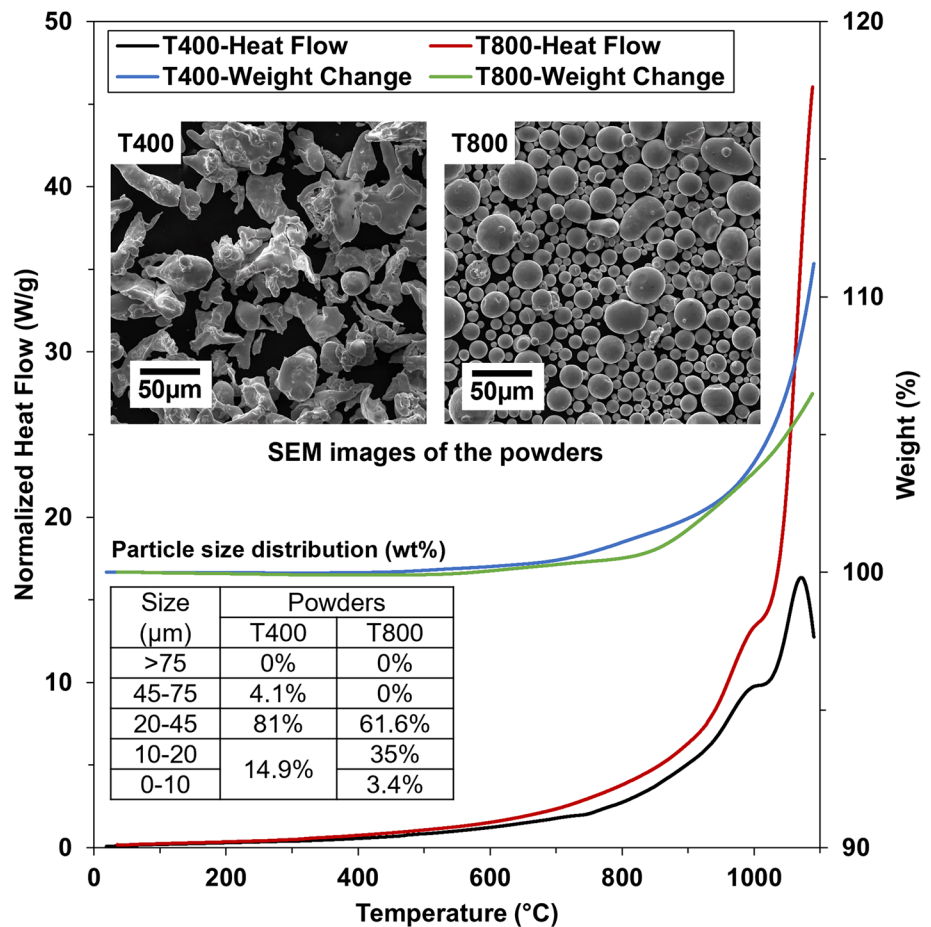
3.1 Powder Properties

Figure 1 shows the TGA and DSC graphs, particle size distribution, and SEM images of T400 and T800 powders. The thermal analysis was carried out to determine any differences among the powders under the influence of heat, up to the heat treatment temperature of 900 °C, in the aspects of oxidation behavior or phase transformations. Moreover, both powders showed a similar trend. At 900 °C, the weight gains are nearly identical, and after about 400–500 °C, T800 yields a slightly higher heat flow than T400. Other than that, no glass transition or phase transformation behavior is observable for both powders. Due to differences in production methods, powder grains show different morphologies and a slight difference in particle sizes. Like the elemental concentration presented in Table 1, the particle size distribution specified in Fig. 1 is directly taken from the certificate of conformity supplied by the manufacturer. This table shows that 80% of T400 remains in the 20–45 µm range, which is 62% for T800. In contrast, 38% of T800 remains below the 20 µm range, and T400 has 15% in this interval. The majority of the particle size distribution of these powders is shifted slightly, with T400 being higher. To simplify the argument, assuming the powders have a normal particle size distribution among all specified intervals, the average particle size values were calculated to represent the variance among the specimens with a single value. Accordingly, the average particle sizes become 30 and 25 µm for T400 and T800, respectively. As the 1:1 mixture of T400 and T800 powders, an intermediate thermal behavior and particle size of 27.5 µm is expected for the third mixture of Tmix. It is also worth noting that in-flight particle interactions are also critical. According to the flame parameters, it becomes possible for individual particles to get in physical contact with neighboring ones, resulting in fusion between the particles, which becomes effective on both the morphology and the resultant average particle sizes [36]. Furthermore, in-flight interaction could well have different effects on different intervals causing a higher degree of modification at that section.

Table 2 The codes of specimens

Alloy	As-coated	Heat-treated
T400	T4-AC	T4-HT
TMix	TM-AC	TM-HT
T800	T8-AC	T8-HT

Fig. 1 TGA–DSC graphs of powders T400 and T800 embedded with SEM images and particle size distribution



3.2 Heat Treatment

The heat treatment process used in this study was based on previous research that explored the impact of annealing at temperatures ranging from 800 to 1000 °C on Co-based Tribaloy coatings [28–30]. The initial selection for the annealing temperature was 900 °C, and the temperature and soaking time were confirmed through DSC and X-ray analyses to determine their applicability. During the DSC analysis of the as-sprayed coatings T4-AC, TM-AC, and T8-AC, crumbled pieces were analyzed, and the data is presented in Fig. 2. The results showed that all three alloys exhibited similar behavior with minimal differences, beginning with an exothermic reaction at 400 °C and continuing up to 1300 °C, with no sign of melting or significant discontinuity. The gradual change in heat flow indicated continuous crystallization of the alloys with increasing temperature. Based on the results, it was confirmed that the beneficial impact of heat treatment only occurs at temperatures above 600 °C, as previously shown in studies [26, 27, 30], and that the alloys retain their stability at 900 °C and exhibit significant heat flow, making this temperature suitable for this study's purposes.

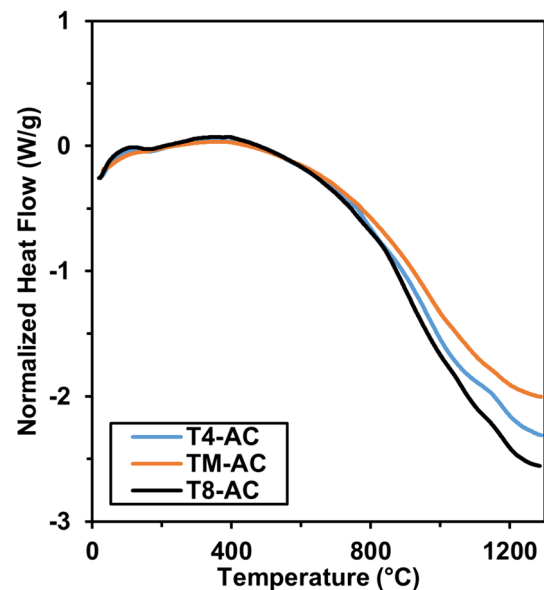


Fig. 2 DSC graphs of as-sprayed coatings

The microstructure's response to different soaking times was assessed by analyzing X-ray spectra after annealing for varying durations. Samples were annealed for 1, 2, and 4 h, and their X-ray spectra were compared. To establish a baseline, initial trials were conducted on T4-AC coatings, which were expected to yield similar results to TM-AC and T8-AC due to their comparable DSC outputs.

As the main intention of the study is to see the effects of the of temperature after a relatively long exposure, to build a determinable contrast between the as-sprayed and annealed conditions, allowing crystallization and solid-state

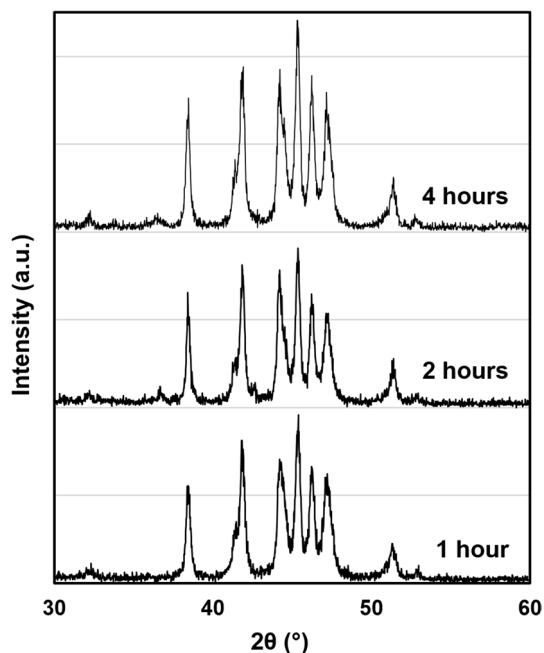


Fig. 3 X-ray spectra of as-sprayed T400 coating obtained after various annealing times

diffusion sufficient time; annealing trials of 1 h, 2 h and 4 h were carried out. As the control unit, the initial trials were done on coatings of T4-AC. With their similar DSC outputs any result obtained from T4-AC was expected to be similar to the specimens TM-AC and T8-AC.

The specimens subjected to X-ray analysis after being annealed for 1, 2, and 4 h displayed significant and identical peaks in their X-ray spectra. Of greater significance, however, is the observation that the majority of peaks exhibited a significant increase in intensity after 4 h of annealing time, despite the similarity in intensities at 1 and 2 h (as shown in Fig. 3). It should be noted that the X-ray studies will be elaborated on in subsequent sections, and that this image serves only to demonstrate the difference in intensities without identifying the phases. Comparison of these spectra with the results of DSC analysis suggests that crystallization continues to occur at longer soaking times, leading to a relatively higher degree of crystallization after 4 h of annealing compared to both 1 and, more importantly, 2 h.

Considering the persistence of crystallization, soaking time was chosen to be 4 h. This was made to facilitate a discernible differentiation between the as-sprayed and annealed conditions, thereby enabling an adequate timeframe for both crystallization and solid-state diffusion to occur.

3.3 Micro-structure

Cross-section images of the alloys in both the as-coated and heat-treated conditions are illustrated in Fig. 4. Arrows of different colors mark the various phases that can be differentiated. Specifically, white, yellow, red, and blue arrows indicate splat boundaries, voids, dark nodular phases, and gray phases, respectively, all of which will be characterized below. The simplest structure was observed in specimen T4, whereas specimens TM and T8 exhibited a relatively

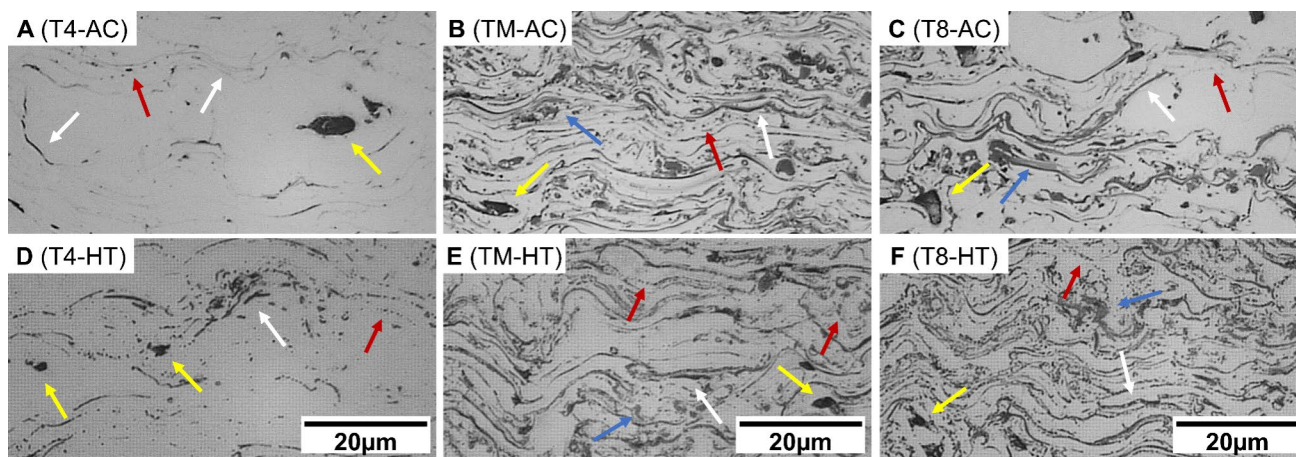


Fig. 4 Optical microstructure of cross-sections of coatings in as-coated and 900 °C heat treated conditions

complex structure with significantly higher splat boundary density. The gray phases highlighted by blue arrows were only visible in specimens TM and T8. After heat treatment, the presence of dark nodular structures shown with red arrows increased significantly, and splat boundaries lost continuity and turned into dashed curves. SEM images of the surface of specimens TM-AC and HT (Fig. 5) revealed these phases and changes under SEM imaging.

Notably, the phases shown with blue arrows are difficult to distinguish in SEM compared to optical microscopy. Nonetheless, all other elements are visible. Additionally, with higher level of detail the disappearance of boundaries of lower contrast in Fig. 5A, and the distinguishable dashed structure of splat boundaries after heat treatment in Fig. 5B are highlighted. Morphologically, this change shows

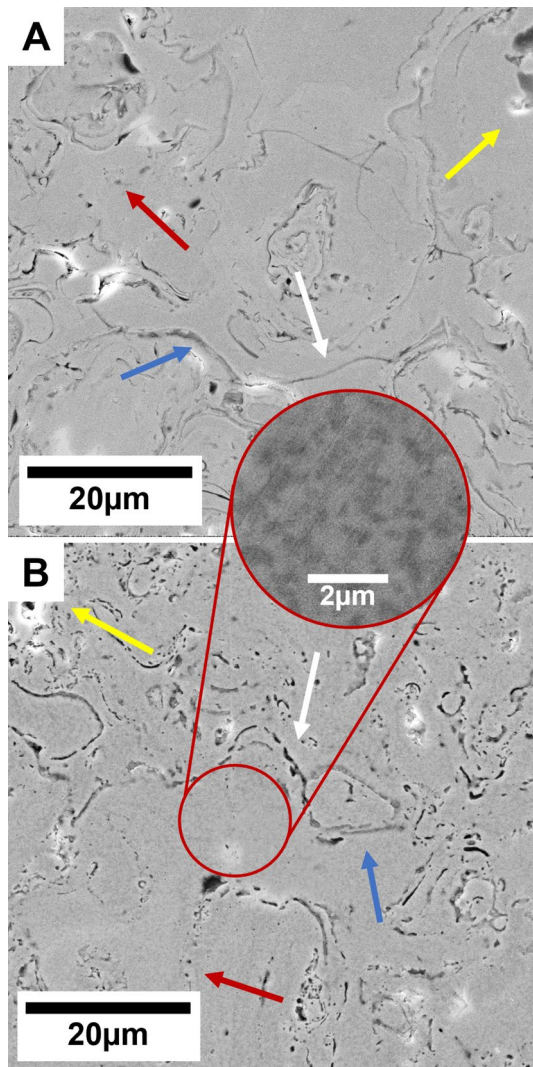


Fig. 5 Surface SEM microstructure of specimen **A** TM-AC and **B** TM-HT with a magnified section of matrix of annealed specimen as the insert

a remarkable similarity to the change observed previously, in the cold-sprayed coatings under the influence of heat treatment [37] which resulted in the closure of splat boundaries and cracks. Similarly in our case, these findings point out crucial evidence for solid-state diffusion bonding across the splat boundaries. Furthermore, Fig. 5B shows that the distribution of black nodular phases is commonly related to splat boundaries. The presence and characterization of these phases will be detailed in following sections. It is also worth noting the formation of a pattern of darker and lighter sections in the matrix after heat treatment, as shown in the insert of Fig. 5.

The dark and light regions of the matrix pattern have been analyzed through EDX analysis, which has shown the specific composition changes in all three alloys. The light regions, marked as X in Fig. 6A, are rich in Mo and Si, while the darker regions, marked as Y in same figure, have higher concentrations of Co and Cr compared to their initial concentration. As discussed in previous literature [38], the elevated concentrations of Mo and Si in the local area suggest the presence of Laves phases, while the increased levels of Co and Cr indicate the formation of a Co-based solid

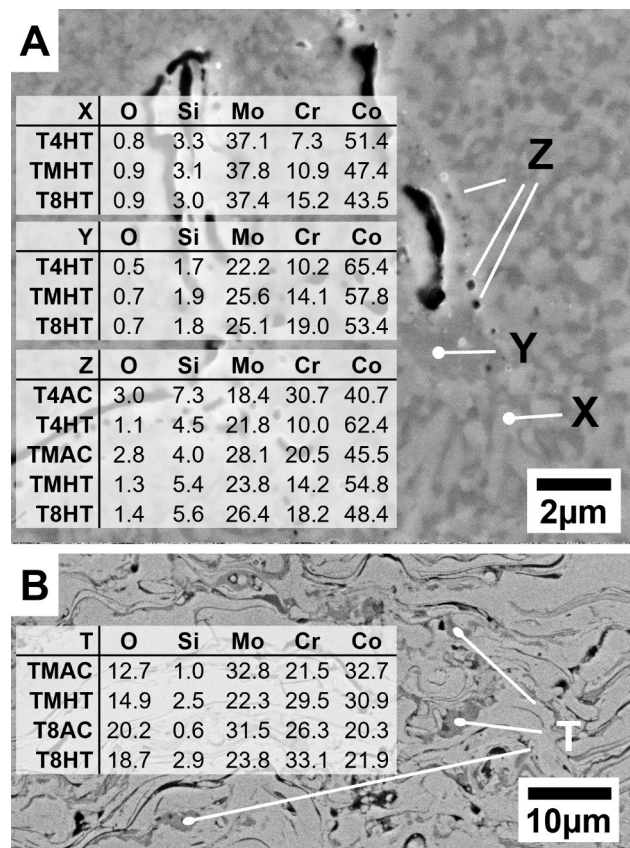


Fig. 6 EDX analysis results various regions specified in the microstructures shown on SEM images of **A** surface and **B** cross-section of TM-HT and T8-AC respectively

solution. Triballoys, in their cast form, are hypereutectoid solutions with a primary Laves phase in Co solid solution. Upon heat treatment, the as-sprayed alloy tends to attain equilibrium, which is evidenced by this locally accumulation of elements. This observation supports significant diffusion within the structure and the notion of diffusion bonding.

Additionally, areas denoted as Z and indicated by red arrows in Figs. 4 and 5 are not significant in the as-sprayed state and can be difficult to differentiate from other constituents. However, meaningful EDX data was obtained from these regions in AC conditions, revealing a drastic increase in Cr and Si (Z in Fig. 6A). After undergoing heat treatment, unlike in AC conditions, significant differences in composition were not easily observable. Nevertheless, these regions consistently exhibit increased Si levels, almost twice the original concentration. Wang et al. [31] showed that the neighborhood of inter-splat boundaries in plasma-sprayed coatings had significant accumulations of Cr (62 wt%) and Si (14 wt%), forming distinct phases of approximately 5 μm or larger. Guo et al. [29], replicated these findings and also found significant enrichment of Cr (26 wt%) and Si (53 wt%) in the same regions after annealing at 800 $^{\circ}\text{C}$ for 1 h, with a morphology similar to the present study. Both studies identified these regions as CrSi_2 Laves phases. However, it is not expected to observe large CrSi_2 phases with any alloy composition under consideration in this study after heat treatment, based on the Cr–Si binary phase diagram [39], since CrSi_2 requires approximately 50 wt% Si. Considering the resolution of EDS and the size of the inspected region being below 0.5 μm , increased concentration of Si was still observable when it was highly possible to collect data from neighboring regions of the surface or thickness. Consequently, these findings support the presence of Si with relatively higher values in these particles. The elemental concentration of Cr would be sufficient for the formation of CrSi_2 in the majority of coating, but the formation of this phase in relation to splat boundaries suggests a significant accumulation of Si in these sections. Furthermore, as a successful repetition of the findings of the studies mentioned above [29, 31], CrSi_2 particles are significantly denser in the neighborhood of the splat boundaries. Especially when in a particular region, higher volume of splat boundaries come together; at these sections, the density of CrSi_2 further increases. Such examples can be seen in Fig. 4D–F. In addition to splat boundary cohesion, elemental diffusion across the splat boundaries also favors the formation of CrSi_2 particles.

Finally, in regions T in Fig. 6B, a significant amount of oxygen and Cr were detected. These Cr–O regions exist in both heat treatment conditions for specimens TM and T8 but their presence cannot be evidenced in the specimens T4-AC and T4-HT. Their absence in the lowest Cr concentration suggests that these sections are mainly Cr_2O_3 .

It is also expected to encounter Co and Mo oxides in the specimens but they also don't show any contrast in both optical and SEM images. It is judged that with higher oxygen affinity of Cr with respect to Co in the melt [40], only increased Cr concentration results in observable oxidation in the structure.

The X-ray spectra of powders and coatings are displayed in Fig. 7. In the 40 $^{\circ}$ –50 $^{\circ}$ range, both powders exhibit a crystallized pattern of phase composition consisting mostly of CoMoSi , $\text{Co}_3\text{Mo}_2\text{Si}$, and Co_7Mo_6 . These phases display heightened intensities in T800 powders. As will be explored further, a decrease in Co concentration results in an increase in the volume of the Laves phase in the structure, which is also evident in the difference in powder spectra. In contrast to powders, coatings reveal a predominantly amorphous structure with a broad hump between 40 $^{\circ}$ and 50 $^{\circ}$ and a few small peaks. This suggests that during spraying, powder particles were fully melted, and rapid cooling rates hindered crystallization to a greater extent. Upon annealing, significant crystallization occurs in all coatings, forming a more complex structure than in the original powder forms. All three alloys exhibit peaks at nearly identical diffraction angles with some discernible intensity differences. The phases identified are consistent with previous studies [29, 30, 41], with the presence of Co_3Mo , Mo_3Si , and CrSi_2 in addition to the previously mentioned phases. Upon careful consideration of the relevant data, it has been observed that both X-ray and EDX analyses yield consistent findings.

The phase analysis done on optical images quantitatively measures the phase changes in all specimens. The change in density of the constituents in the coatings is significantly visible in the surface microstructures, as presented in Fig. 8A, and the results can be seen in Fig. 8B. Since the measurements also include the voids in the coatings, the total ratio of the voids measured from the cross-sections of the coatings was also integrated into the column chart in Fig. 8B.

In all coatings, average porosity levels were in the range of 0.5%, which showed a reduction of 0.1% after heat treatment in all specimens. Remelting or partial remelting of the coating by heat treatment or other methods reduces the number of voids and increases the bonding strength and integrity [30, 31, 33–35, 42]. Similarly, the voids and cracks were examined to be cured by the effect of diffusion bonding after annealing [43–46]. As can be seen in Figs. 1 and 2 and by examination of the binary and ternary phase diagrams of Co–Mo–Cr–Si element combinations in literature [39, 47–49], no melting is expected during a heat treatment at 900 $^{\circ}\text{C}$. The primary mechanism of porosity reduction is considered to be solid-state diffusion bonding, which is already present in Fig. 5. Moreover, a reduction of 0.1 is a meaningful difference expected from the diffusion bonding process. Furthermore, it was concluded that similar porosity values remaining less than 1% in all specimens will not be

Fig. 7 X-ray spectra of powders and specimens in as-sprayed and heat-treated conditions

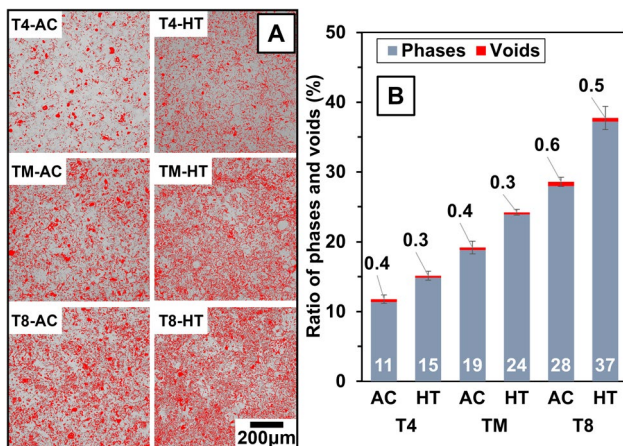
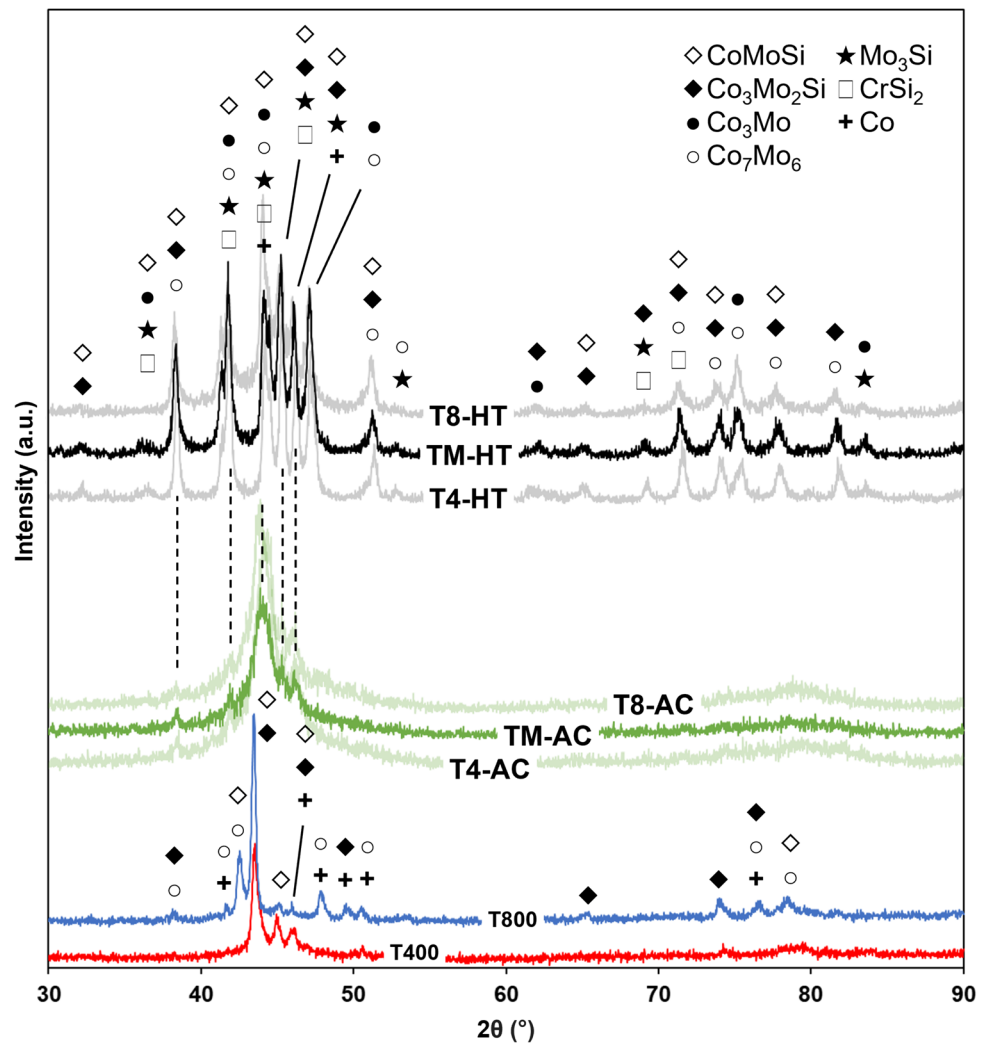


Fig. 8 **A** Phase painted surface optical microstructure images of all types of specimens and **B** area percent of phases

the decisive factor in any variation of the mechanical and wear performance of the specimens.

Despite some observable differences in porosity concentration, it was determined that average values of 0.5% were also not decisive for remaining phase ratios in general. As previously mentioned, the splat boundaries are the primary components of as-sprayed specimens. While TM and T8 display the formation of Cr_2O_3 (T in Fig. 6B) in addition to the splat boundaries, they are less visible in surface view compared to the cross-section. Therefore, the phase ratio measurements of AC specimens mainly indicate the amount of inter-splat boundaries in the structure. Following heat treatment, there was no change in the presence of Cr oxides, but as described previously, heat treatment causes the formation of CrSi_2 in all types of specimens. Thus, the primary difference in the phase measurement results between the AC and HT is the formation of CrSi_2 . Consequently, considering the results of AC specimens, as the particle size reduces in the order T4-TM-T8, the ratio of the inter-splat structure shows a nearly linear and constant increase of 8%–9% among the

specimens with the opposite order. However, with the application of heat treatment, an increase in phase ratio of 4, 5, and 9% occurs, respectively, for specimens T4, TM, and T8, which, as stated, corresponds to the formation of CrSi₂. The increase in Cr is linear among the three alloys, but CrSi₂ shows an exponential increase, nearly doubling between TM and T8. These findings align with the previously mentioned mechanism of CrSi₂ formation in relation to splat boundary density and the presence of Si in these areas. As a result, the heat treatment process promotes the formation of CrSi₂ due to the increased splat boundary density.

3.4 Mechanical Properties

Micro-hardness test results and hardness indentation images are given in Fig. 9A, B, respectively. Considering the HV0.3 results, in the as-coated state, there is a decreasing trend in hardness in the order of T4, TM, and T8, and the difference between average values are between 61 and 31 HV0.3, corresponding to 5%–8% of the individual results. The indentation images reveal a significant surface breakdown in the neighborhood for AC specimens (Fig. 9B). Some detachments (white arrows) and cracks (red arrows) form during the test, which makes it difficult to distinguish the edges of the indentations. After heat treatment, the surface dissipation significantly reduces (Fig. 9B). Some detachments were observable at lower degrees compared with the AC state. After heat treatment, a significant hardness increase was observed with respect to the AC conditions, with T4 and TM showing very close values and T8 becoming the hardest among the three alloys. Considering the possible effects of cracks around the indentations on the test results, another set of test with a proportionate yet lower scale of HV0.1 was conducted to obtain results without breaking the surface. Even though still some fractures were present after HV 0.1 indentations, their ratio was significantly lower, and furthermore it was possible to obtain sufficient number of intact indentations to obtain reasonable results. This way, a better test successfully representing the hardness of the microstructure without the effects of fractures was done.

With HV0.1, in both AC and HT conditions, a different trend with higher hardness results was observed (Fig. 9A). This time, a gradual increase was obtained in the order T4 < TM < T8 in both AC and HT states. In AC, this increase remains in the range of 4%–7%, but after heat treatment, this difference doubles, reaching 14%. Comparing the AC and HT states, a gradual increase of 11, 18, and 30% was observed, respectively, for specimens T4, TM, and T8. As mentioned in an earlier review study [50], increasing the Mo/Co ratio results in a higher degree of hardening by allowing a higher degree of Mo-based Laves phases in the structure. In addition to increased amounts of Mo, the presence of Si favors the formation of Laves

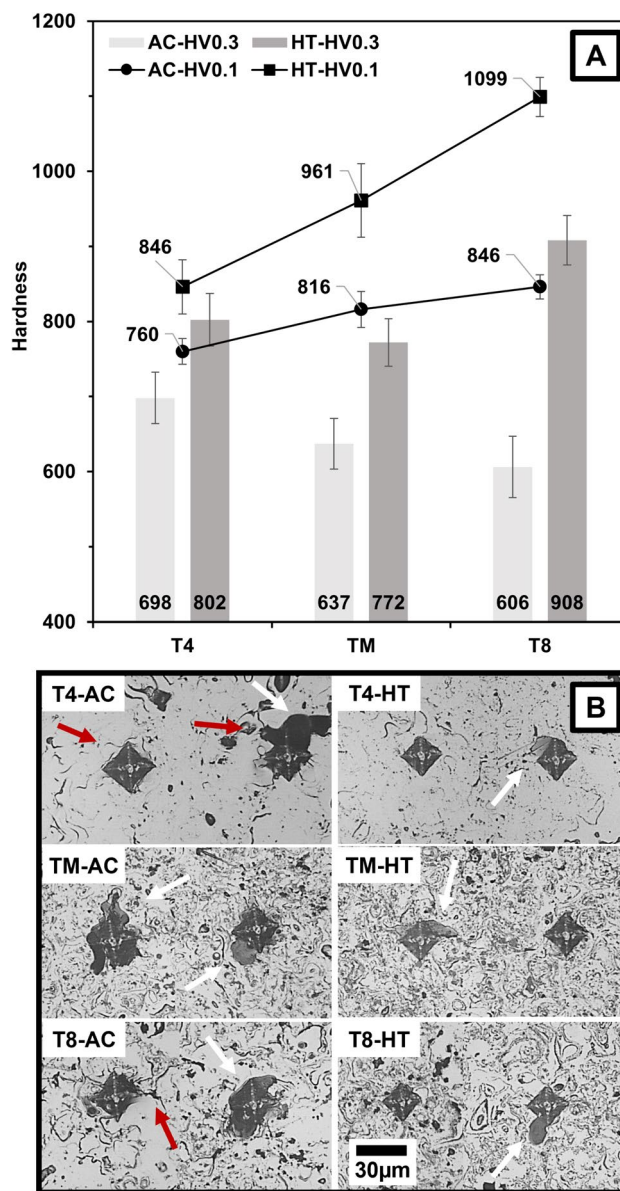


Fig. 9 A HV0.3 micro-hardness test results and B optical images of hardness indentations

phases [41, 51]. In our case, as the Co concentration gets lower among the specimens, the relative amounts of both Mo and Si increase in concentration, which forms higher amount of Laves phases with increased hardness. As-sprayed specimens are also capable of producing higher amounts of Laves phases as Co concentration gets reduced in the alloys but after annealing, as described previously, formation of Laves becomes more significant and change in hardness becomes more pronounced. Moreover, the difference between trends of HV0.3 and HV0.1, show that surface integrity significantly influences mechanical properties which will be explored with scratch testing.

The use of scratch tests provides reliable information regarding the coating integrity. Figure 10 displays SEM images that illustrate the surface topography of the tested specimens. The as-coated specimen displayed brittle behavior with significant cracking, while the heat-treated specimens exhibited a trace embedded with cracks that had undergone plastic deformation. As the indenter traversed, significant crack formation persisted in the as-coated specimens, resulting in a surface covered in cracks. Conversely, in the heat-treated specimens, while some cracks emerged in the initial stages of testing, there existed regions free of cracks. Beyond the midpoint, the frequency and severity of cracks increased, yet still remained notably less than the as-coated specimens.

The transition between the surface and scratch geometry leads to cracks of higher significance at the edges in all specimens, as shown in Fig. 11A. This effect is more pronounced in the as-sprayed condition, which shows a higher degree of brittleness, causing cracks to protrude from the indenter contact area and dissipate in close neighborhoods. In contrast, plastic deformation with fewer cracks is observed in the annealed state. Further magnification (Fig. 11B–D) reveals that the cracks are mostly related to inter-splat boundaries, which become more apparent at the edges of the traces for the AC specimens. These cracks make branches perpendicular to the scratch direction through the center of the scratch, which are sparse in T4-AC (Fig. 11B) and have highest density in T8-AC (Fig. 11D), and TM lies in between.

Figure 12 provides a closer look at the cracking behavior of the specimens, with yellow arrows indicating separated splat boundaries and red arrows showing cracks originating from the tips of these boundaries. The structure of the splat boundary separation indicates a torn structure, while the rest of the cracks display brittle characteristics with no deformation at the opposing edges. As seen in the same image, cracks originating from the splat boundaries (yellow arrows)

produce some curves with no relation to the indenter direction. However, brittle cracks shown in Fig. 12A, B which propagate perpendicular to the indenter direction are cracks originating from the tips of the separated boundaries (red arrows). Having interconnected cracks with different characteristics suggests that splat boundaries act as stress concentrators and favors initiation and propagation of other cracks and these propagated cracks reaches to the other separated boundaries and forms a crack network. This behavior is significantly visible in Fig. 12B.

Upon thorough examination of the heat-treated specimens, noteworthy improvements became apparent in the cracking behavior. As demonstrated in Fig. 13A, similar to the as-sprayed specimens, cracks were observed originating from the splat boundaries, indicated again by yellow arrows. Even though other separated boundaries were nearby, heat treatment prevents further propagation and separated boundaries remain disconnected. This effect was particularly evident in the region indicated by the blue arrow where two separated tips were 2–3 μm apart and remained disconnected (Fig. 13A). In the upper sections of Fig. 13B, this behavior was even more accentuated. All cracks followed splat boundaries and, despite a higher boundary density, they remained mostly disconnected. However, the crack marked by the red arrow exhibited similar brittle characteristics seen in the AC specimens. Although significant evidence of increased toughness is visible with the effect of heat treatment, few brittle cracks still exist.

For further understanding the variation of cracking behavior, analysis was quantized by determining the critical force for cracking and measuring the crack density. Critical force for cracking, the force required to initiate the earliest crack in the scratch trace, was taken as a representation of bonding strength of the coatings. The initial cracks were detected using the SEM images presented in Fig. 10 and measuring their distance from the beginning of the trace

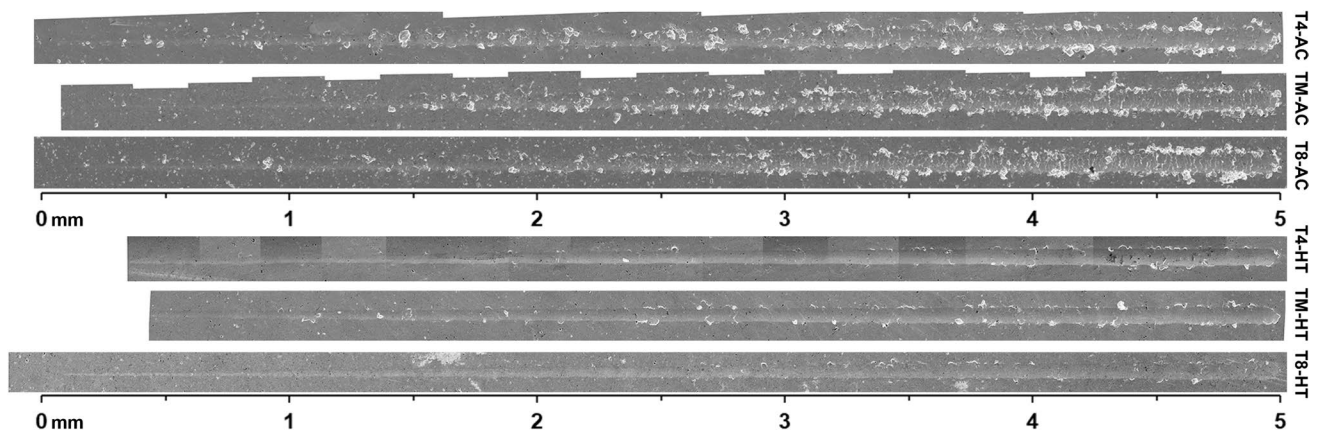
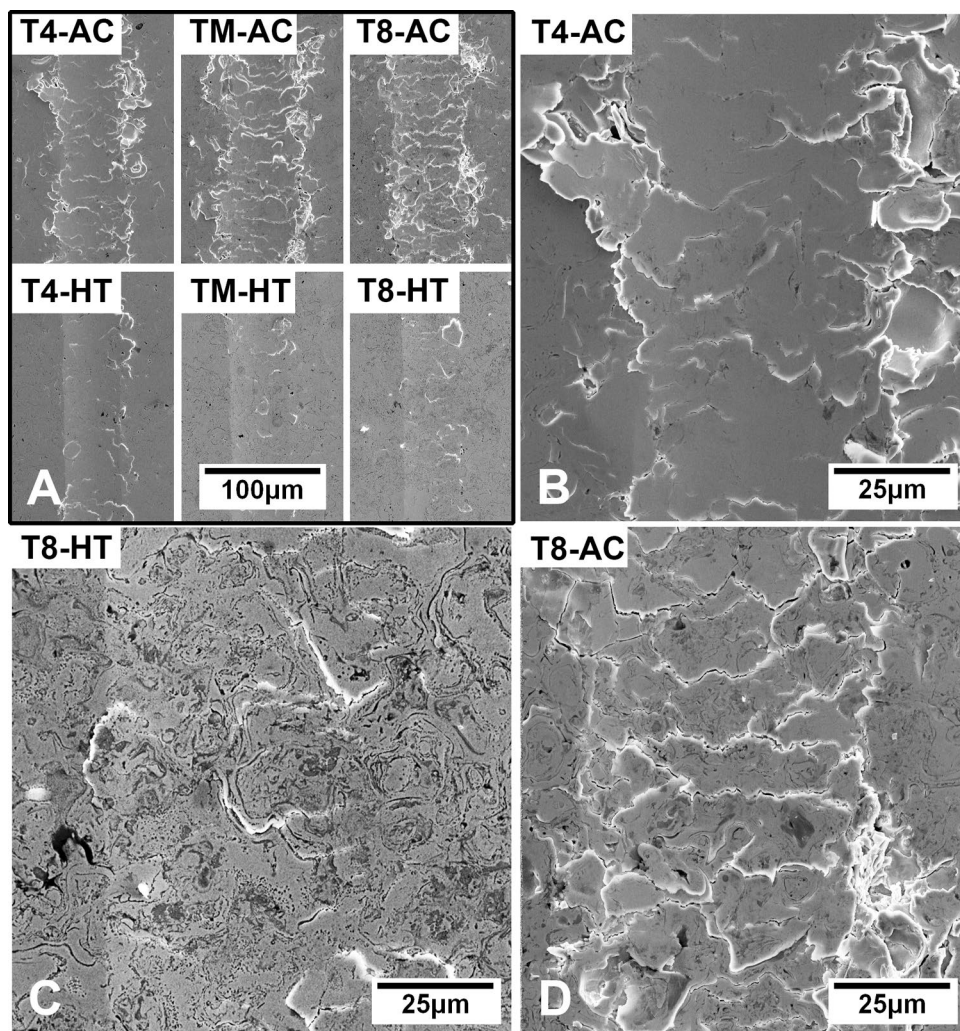


Fig. 10 SEM images of micro-scratch traces of specimens in AC and HT conditions

Fig. 11 SEM Images of **A** general view of mid-sections of micro-scratch traces of all specimens and **B** T4-AC, **C** T8-HT and **D** T8-AC at higher magnifications

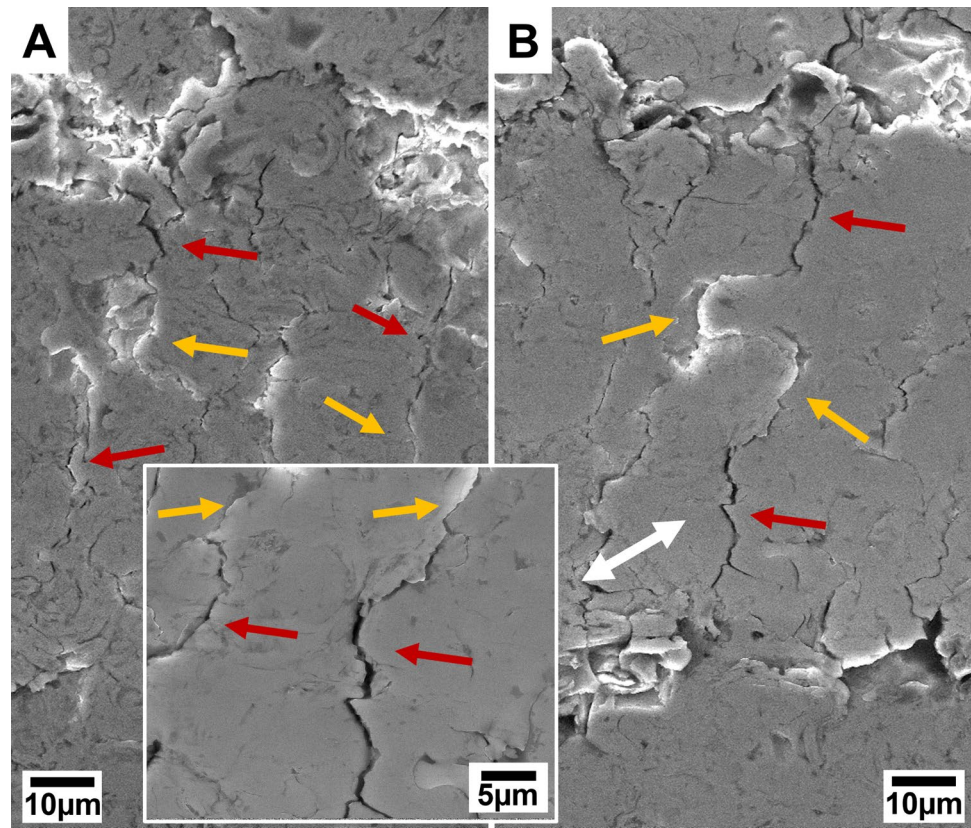


the force at that point was calculated. Results for critical force for cracking is presented in Fig. 14B. According to this figure as-sprayed specimens forms first cracks at 0.5–1.1 N interval whereas this increases to 2.9–3.4 N after annealing. Considering these results, it is revealed that the bonding strengths in as-sprayed and heat-treated states are very similar among each other and heat treatment provides an increase of approximately 4 times. Moreover, results contain relatively high measurement errors, up to 50% for the AC-specimens and 15%–20% for the HT-specimens. For instance, for the specimen T4-HT having the maximum error of 0.7 N, it takes the indenter to travel 175 µm to generate this difference. Since cracks were mainly related to the splat boundaries, during the travel of indenter upon a weaker boundary at the slightly earlier stages or slightly later stages can well change the initial crack location. Thus, no meaningful relation can be built regarding the alloy concentration or average hardness values for the HT and AC specimen sets.

Additionally, general cracking behavior throughout the entire scratch trace was observed by counting the number of

cracks. To obtain the crack count, a line was drawn through the center of the traces, and all cracks that intersected these lines were tallied, as demonstrated in Fig. 14D. The findings depicted in Fig. 14A show that as expected, the number of cracks gradually increases in all specimens as the force increases. As the fractographic examination revealed that the cracks are related to the splat boundaries, a correlation between the number of cracks (Fig. 14A) with the splat boundary density (Fig. 8B) becomes logical. In AC condition, the boundary density increases almost linearly in among the specimens (Fig. 8B), however, when the total number of cracks are compared, an exponential trend is observable. T4 and TM showed very similar values up to a distance of 3 mm, but beyond that point, the number of cracks in specimen TM slightly increased compared to T4-AC. Among these specimens T8-AC shows significantly higher number of cracks through the whole length. Among these specimens, boundary density and hardness increase in the same order as $T4 < TM < T8$. Again, parallel to the fractographic examination, as the splat density

Fig. 12 SEM images of scratch traces of specimens **A** TM-AC and **B** T8-AC at higher magnifications with respect to Fig. 11 showing lower central section of T8-AC as an insert in greater detail



increases, the distance between two boundaries reduces and it becomes easier for cracks to propagate from one boundary to the other. Furthermore, in the amorphous structure since the increase of hardness is related to the formation of higher amount of Laves phase, increase of hardness points to increased brittleness with absence of Co-based solid solution. Combination of these two factors show an increased cracking vulnerability in specimen T8-AC.

On the other hand, annealing heat treatment led to a dramatic decrease in the number of cracks, regardless of the alloy concentrations. Furthermore, they exhibited very similar behavior throughout the test. Figure 14C shows the true crack density at the final and most compelling section of the test. Although we still obtained the highest number of cracks in the T8-AC in this section, it is very close to the results for TM-AC, contrary to what we observed in the whole length. T4-AC shows an important difference at this section, with its lowest boundary density. Heat-treated specimens, unlike the as-coated specimens, exhibit nearly identical behavior in the final 1 mm length, as observed throughout the entire trace.

It is also worth noting that although annealed specimens show very similar cracking density, a comparison with the as-sprayed condition reveals various strengthening levels between the specimens. As the number of cracks of the as-sprayed and heat-treated specimens is compared in the whole scratch trace, specimens yield 88, 88, and 92% reduction

in the number of cracks, respectively, for T4, TM, and T8. These ratios become 80, 84, and 85 in the final 1 mm, again in the same order. Consequently, supporting the above explanations about the phase ratio of the specimens, combining higher density of splat boundaries with an abundance of Cr, a higher degree of strengthening occurs with the effect of annealing heat treatment. Diffusion welds the weaker splat boundaries and simultaneously promotes the formation of hard CrSi₂ particles in close proximity, further strengthening the boundaries.

Furthermore, the total deformed area of the annealed specimens was calculated by measuring the scratch trace widths of heat-treated specimens. The results were 9.96×10^{-3} , 9.80×10^{-3} , and 9.17×10^{-3} mm², respectively, for T4, TM, and T8, which makes a 6%–8% reduction between the specimens. The plastic deformation of the specimens shows a parallel reduction with the formation of CoMoSi, Co₃Mo₂Si, and CrSi₂ laves phases and the strengthening of the splat boundaries.

The fractographic examinations and quantitative analysis of scratch tests conclude that the weakest regions in both as-sprayed and heat-treated conditions are the splat boundaries, originating all cracks. The overall strength of the coatings is directly linked to the strength of the inter-splat boundaries. In the presence of weak boundaries, the integrity of the coating decreases parallel to the density of the splat boundaries.

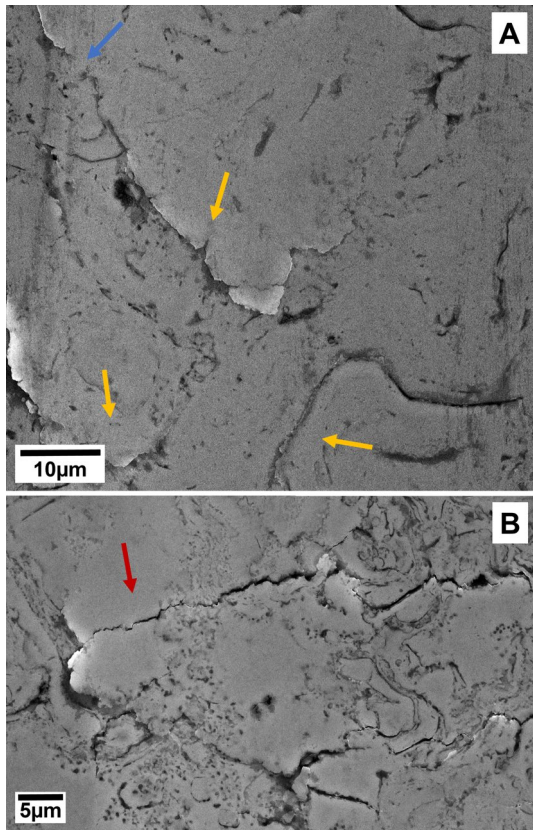


Fig. 13 SEM images of scratch traces of **A** T4-HT and **B** T8-HT

Applying annealing heat treatment shows a solid advantageous difference in boundary strength achieved by diffusion-controlled solid-state welding across the boundaries [38, 43–46]. In our specific case, it was possible to obtain a four-fold strengthening of the splat boundaries by annealing. Additionally, modifying the alloy concentration makes it possible to cure a higher volume of splat boundaries, resulting in a lower number of cracks combined with reduced deformation, resulting in a higher degree of toughness.

3.5 Wear Performance

Figure 15A offers a clear visual representation of the wear scars of all three specimens after room temperature tests. The primary objective of these images is to draw attention to the differences in wear scar topography among the specimens in a more discernible way. In the AC condition, these images reveal significant surface disruption accompanied by abrasive wear, with the level of deterioration increasing in the order of T8 > TM > T4. Further analysis reveals that the topography of the wear tracks exhibits a parallel behavior with the scratch tests, as initially observed. Despite a slight variation in wear ratio, distinguishable yet common sections were detected in all three types of specimens. These shared components indicate that the wear rate is the primary differentiating factor among the as-sprayed specimens after undergoing room temperature tests. To provide

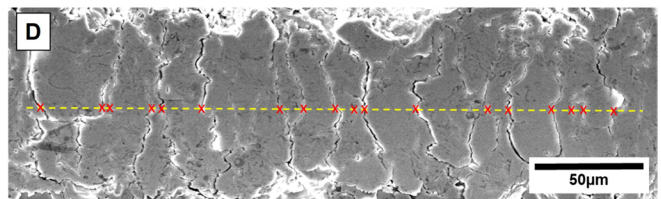
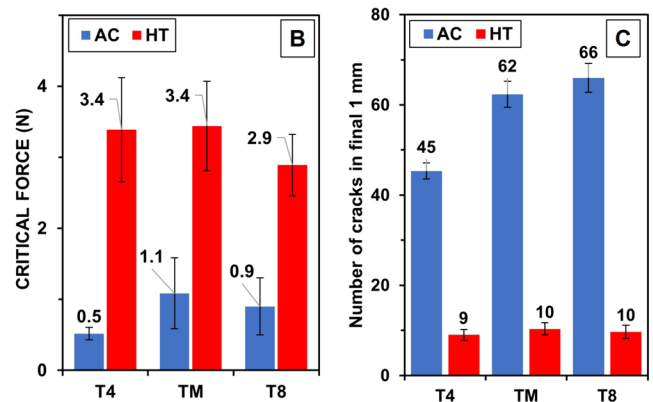
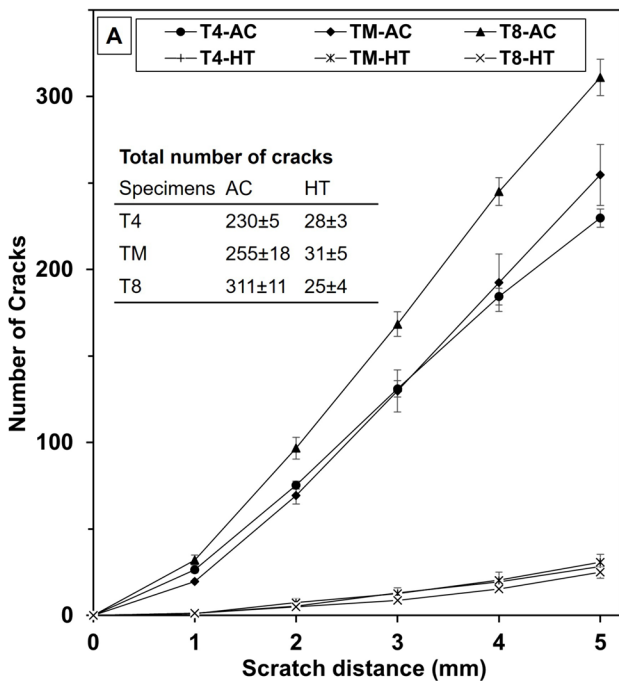
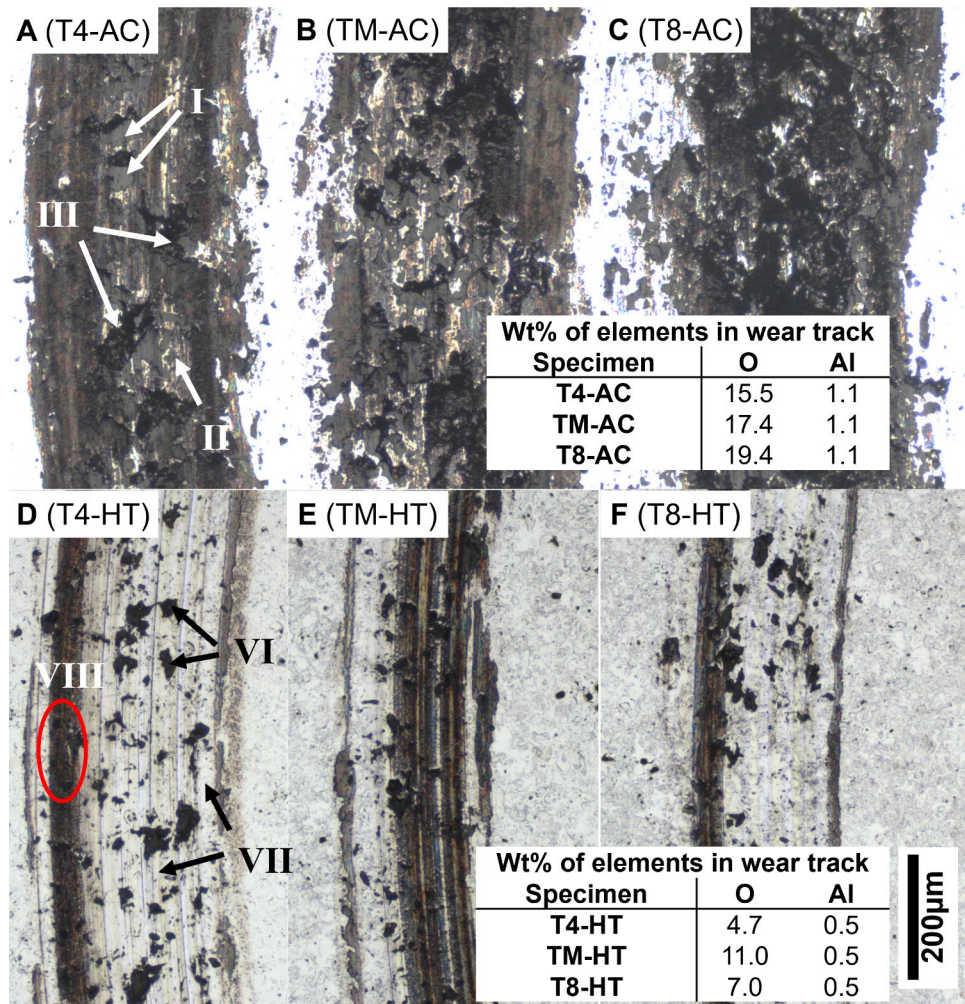


Fig. 14 Graphs of **A** number of cracks versus scratch distance, **B** critical force for cracking and **C** number of cracks in final 1 mm length of scratch trace and **D** illustration showing the crack counting method

Fig. 15 Optical images of wear tracks of POD tests at room temperature



a comprehensive characterization, these components were labeled using Roman numerals.

Moreover, elemental composition of the wear tracks was surveyed and presented in Fig. 15A as an insert. The oxygen content is investigated for signs of tribo-oxidation, while the presence of aluminum for adhesion as indication of remnants of the counter body. Wear tracks show the presence of significant oxygen and some aluminum. The aluminum content remains consistent among all specimens at very low levels. It is worth to note here that it was possible to detect an average of 0.5 weight percent Aluminum in EDX analyses performed on locations away from the wear path. Therefore, it is certain that there is mainly no aluminum residue on the surface, or if there is, the amount is very low. On the other hand, slight and gradual rise in oxygen levels in the specimens indicates an increase in the degree of tribo-oxidation caused by greater surface dissipation. The resultant effect of this change will be examined while discussing the friction behavior.

Compared to the as-sprayed coatings, the wear tracks of annealed specimens exhibit lower oxygen concentration and

greater variation in values and again the aluminum content is negligible (Fig. 15B). Upon further inspection, it's evident that the sliding procedure creates a banding effect on the surface with higher oxygen content, which ultimately determines the wear track's total oxidation behavior. Figure 15B also illustrates that the thickness of these bands varies from specimen to specimen and location to location, resulting in a fluctuation of the wear track's total oxygen concentration depending on the location of the EDX analysis. These bands will be detailedly investigated in following sections.

In Fig. 16, magnified images of wear tracks, which have been marked to correspond with the regions in Fig. 15 can be seen. EDX analysis results are also presented for these regions below the images, which provide valuable findings. As clearly seen from this image, after wear, the surface becomes composed of constituents having different topographies and oxygen and aluminum concentrations. As three elements, regions marked as I, II and III construct the main structure of the wear topography. Region I, has the highest oxygen concentration among other constituents and aluminum reaching 2 wt% and they reveal very close Co and

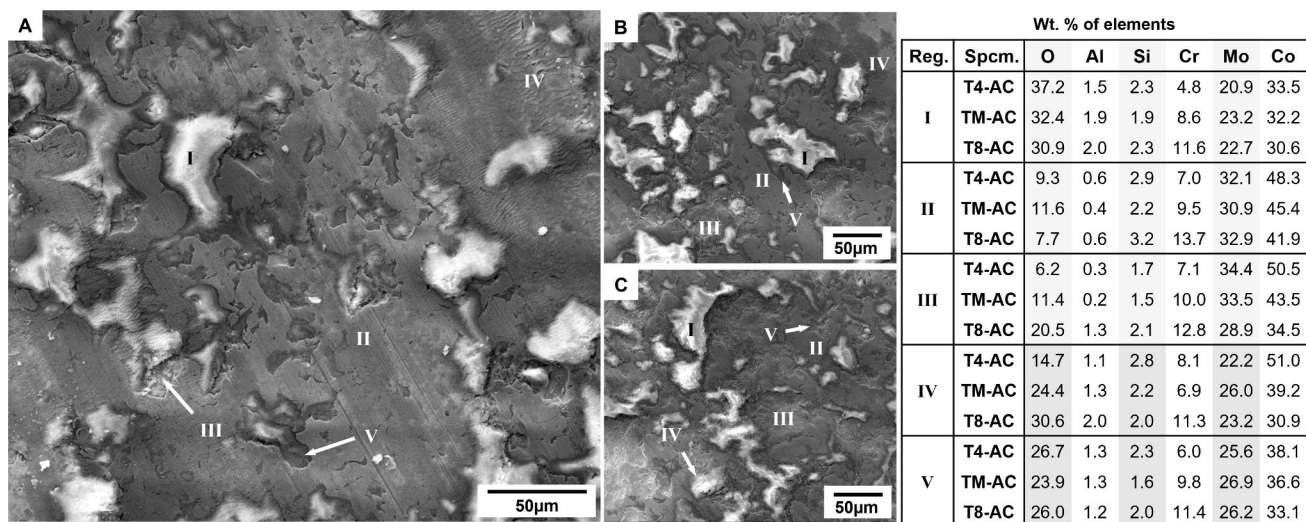


Fig. 16 SEM images of pin on disc wear tracks of as-coated specimens **A** T4, **B** TM and **C** T8 for test at room temperature and EDX analysis results of all the phases that are marked on images

Mo values in all three alloys. The topography, elemental concentration and the presence of these elements are well in line with the findings related to Co_7Mo_6 particles that were specified in the previous study carried out by Guo et al. [29]. These hard particles remain attached to the surface and endure the whole wear process in all three alloys. According to the findings of same study [29], Co_7Mo_6 undergoes oxidation to form CoMoO_4 . This transformation may occur during wear at room temperature, when localized high temperatures are present [27]. As surface dissipation increases, the surrounding sections of this phase are removed, and Co_7Mo_6 particles come into direct contact with the pin during testing. This leads to greater oxidation of the particles. Moreover, an increase in the Mo/Co ratio would favor the formation of Co_7Mo_6 and increase the number of particles, similar to the formation of the Laves phase. The effectiveness of this phenomenon was observed to vary with the oxygen concentrations of the specimens.

Regions marked with number II have some oxygen and very close elemental concentration to the initial alloys, which suggests they are mainly intact sections with some tribo-oxidation. The plowed topography suggests the presence of some abrasive wear in these sections. Regions marked as III are detached zones. They are present in all alloys, and their oxygen concentration shows variations among them. EDX data is collected from the remaining coating layers underneath the initially detached components in these sections.

Additionally, the oxidation rate of the newly exposed layer after detachment will differ based on the test stage at which it occurred. A comparison of images in Fig. 16A–C confirms the initial observation made in Fig. 15A about the degree of surface degradation. Magnified images reveal that regions

marked as II give way into III evidencing loss of integrity at varying magnitudes parallel to the crack intensity.

Although having lower presence, the zones numbered IV and V, also appear in every structure. Region IV showed some deformation and formed a wavy structure in the orientation perpendicular to the direction of movement of the pin and some cracks in several locations. They showed higher oxidation than region II and various oxygen contents were detected in all three alloys. Inspecting Fig. 16 reveals that this wavy structure seems to be forming on different components which explains variations in oxidation. Finally, although the regions numbered V look like a unique structure, these also are the sections where detachment occurs. They are very similar to the region III with not as deep and prominent damages.

Following annealing heat treatment, the topographical features of all alloys undergo a near-complete transformation at room temperature and all three alloys reveal similar appearance (Fig. 15B). As illustrated in Fig. 15B surface is composed of black sections, a light surface and a darker band which are numbered VI, VII and VIII respectively. A more detailed view of the wear scar is provided in Fig. 17. In Fig. 17A the banding is very clear and mainly a plastically deformed wear path is observable. A detailed look at Fig. 17B reveals the general structure of the darker band exhibiting a topography similar to the aforementioned wavy structure and additionally, a branched crack network which is clearer at the lighter section partially covering the surface is visible. Again, the elemental concentration of the numbered zones is supplied as an insert in Fig. 17.

It is worth noting that the constituents marked as VI appear to be the same particles numbered as I in Fig. 16. In this test, since the surface remained more robust, these

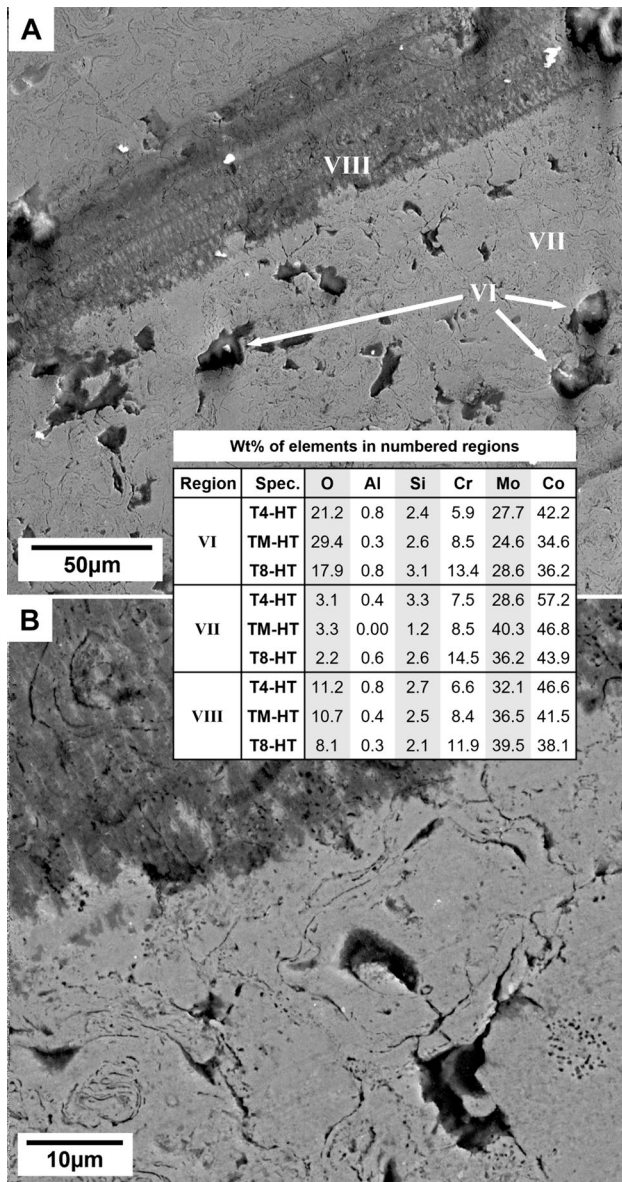


Fig. 17 SEM images of wear scar of specimen T8-HT pin on disc tested at room temperature at **A** lower and **B** higher magnifications. Region VI, VII and VIII are marked on the images and their EDS analysis are given in middle

particles remained relatively hidden and since the frictional load on the particles was shared by the neighboring surface, the oxidation rate remained slightly lower than the AC specimens. Detailed images of particles number VI with higher magnification are presented in Fig. 18 and marked with yellow arrows. In the images the out-of-focus sections shown by yellow arrows represent the pieces of these particles that were broken and removed from the surface during wear. Also, upon close inspection, cracks on the remaining darker sections especially in the particles shown in Fig. 18B are visible. These cracks suggest that as the wear progresses the

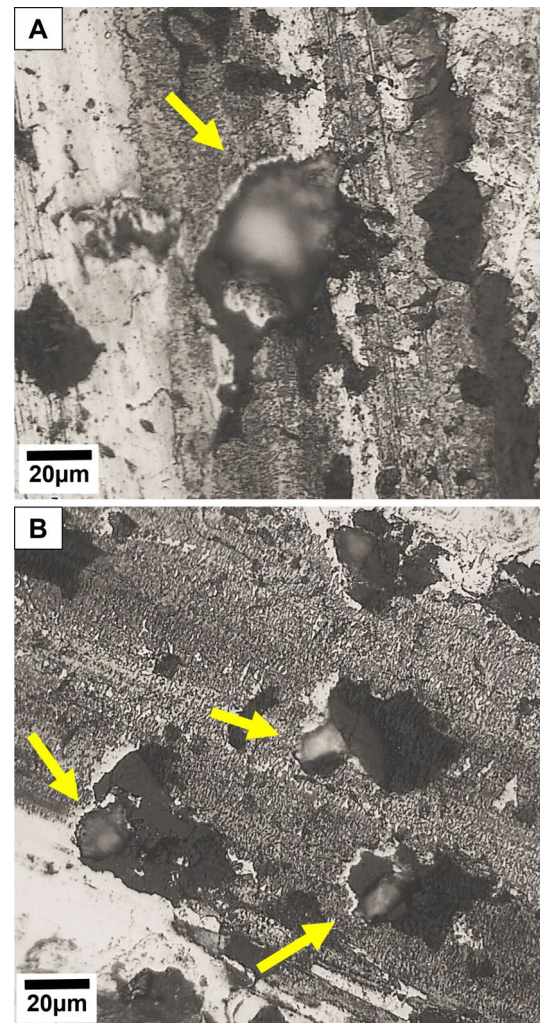


Fig. 18 Optical images of wear scars of room temperature POD tests of specimen **A** T4-HT and **B** T8-HT

individual cracks propagate and make connections forming highly fractured local zones and consequently these regions gets detached from the surface. The significant cracks in Fig. 18B accompanied by small detachments also support this phenomenon. As depicted in the figure, the size of these broken particles can easily exceed 50 µm (Fig. 18A), or it is possible to come across smaller but clustered versions of these fragments in relatively small areas (Fig. 18B). Furthermore, these particles are not uncommon or sparse along the wear circumference in all three specimens. Hence, after annealing, although not comparable to the as-coated specimens, some slowly progressing detachment was observed.

The darker band (marked as VIII), shows some oxidation and conversely, the lighter section (number VII), exhibited very low oxygen concentration. No evidence of aluminum was present in both sections. Even with significant crack propagation during the test, annealed specimens conserve the ability to maintain integrity compared to as-sprayed

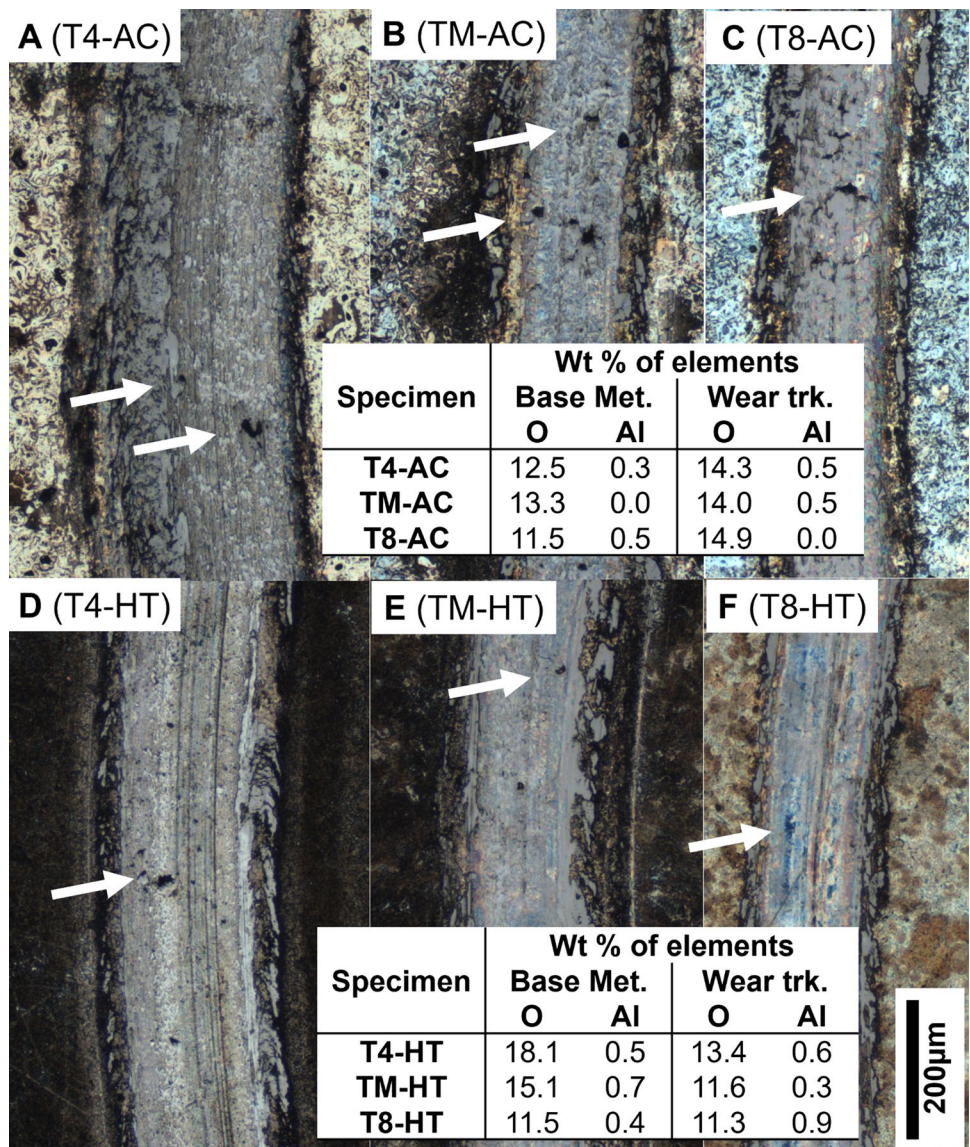
specimens. As in scratch testing, this is another good indication of increased toughness. Additionally, plucking of these relatively larger sections, higher ductility of wear track, and presence of hard Co_7Mo_6 particles embedded in the structure prevent the counter-body from making homogeneous contact with the surface and result in the formation of oxidized areas as bands that show variance along the wear path.

Results from high-temperature tests indicate a very distinct wear behavior compared to room temperature tests, but resultant structure for as-coated and heat-treated specimens are similar to some extent. Images presented in Fig. 19 demonstrate the structure after the high-temperature tests. In these images a more uniform structure with no banding or waves is present. Some plowing is visible. It was possible to rarely encounter detached sections as indicated by white arrows in Fig. 19. EDX analysis of the wear track and locations away from the wear scars (Fig. 19-insert) shows

significant oxygen concentration, which reveals formation of a homogeneous oxide film on the whole surface. As the main difference between the room temperature and high temperature tests of as-coated specimens, the oxide film contributes to the integrity resulting a very dramatic improvement with just scarcely distributed detachments. Moreover, although there were also some dismantled sections of the heat-treated specimens, with a rough observation through the images (Fig. 19) these were determined to be lower than those of the as-sprayed specimens. This further reduction was achieved with the contribution of splat boundary cohesion to the oxidation.

Like in previous steps, different regions were numbered on SEM images (Fig. 20), as IX and X. These individual points show relatively higher oxygen concentrations than the average values of the rest of the structure. These areas on the as-sprayed specimens are separated by more distinct

Fig. 19 Optical images of wear tracks of POD tests at 600 °C



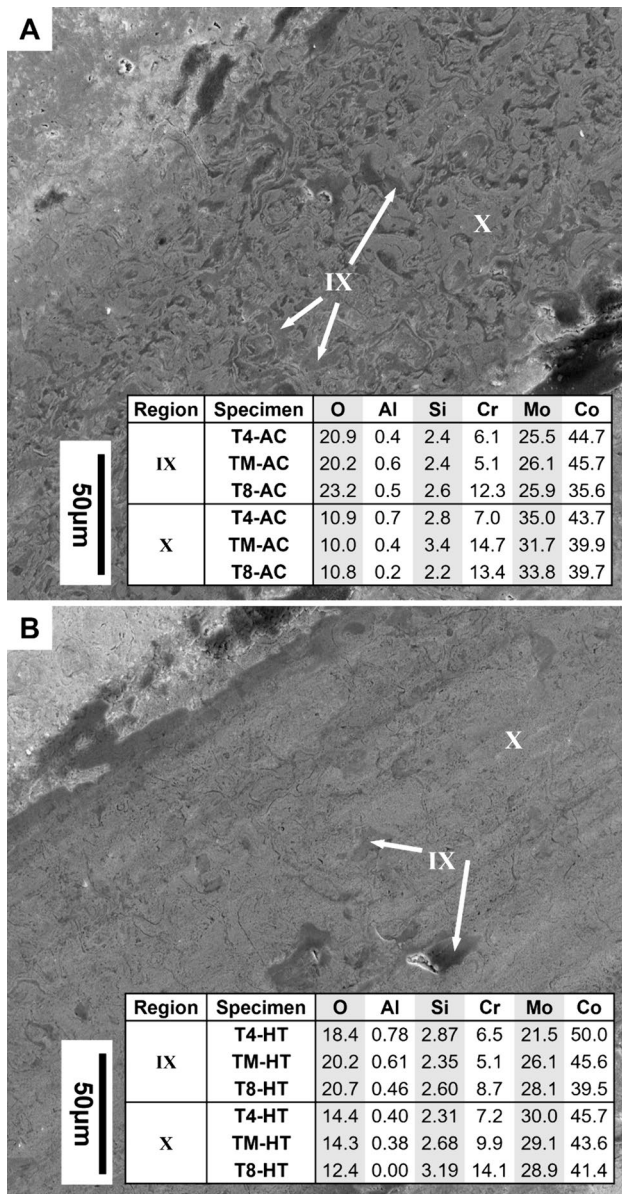


Fig. 20 SEM images of wear scars of specimen **A** TM-AC and **B** TM-HT tested at 600 °C

boundaries compared to the heat-treated ones (Fig. 20A). After heat treatment, the topographical difference between them was found to be very small (Fig. 20B). This relatively heterogeneous structure in AC specimens is a reflection of the multi-component structure detected in room temperature tests. In addition to the different behavior of this structure under wear conditions, it was also revealed that there was a regionally different oxidation behavior at high temperature in these specimens producing a surface composed of a pattern of higher and lower oxide concentration. Elevated temperature tests show that in addition to all mechanical changes, heat treatment also reduces the

regional differences in oxidation tendency and provides the structure with an oxide film of a higher degree of homogeneity.

Further characterization of the locations with high oxygen concentration was done with Raman analysis to pinpoint the oxidation products on the wear surfaces. It is known that the presence and types of oxides play determinant roles on the overall performance of the wear surface. More specifically especially related to Co based Tribaloys, it was found that the Co and Mo oxides are advantageous for their lubricating properties, whereas Cr_2O_3 introduces hardness to the surface [27, 28]. Therefore, the oxidation products on the wear surfaces were investigated to specify any detectable differences among the specimens. The primary emphasis was placed to the elevated temperature test specimens and also higher oxygen-containing bands of room temperature test specimens of annealed alloys. Upon inspection, it was possible to obtain peaks of MoO_3 [52–54], CoMoO_4 [55–59], Co_3O_4 [60–64], and Cr_2O_3 [65–67].

The Raman spectra analysis of the darker bands in wear tracks from room temperature tests showed remarkable similarities, as seen in Fig. 21. The presence of MoO_3 , CoMoO_4 , Co_3O_4 , and Cr_2O_3 was detected. One notable difference among the spectra was observed in the 500–550 cm^{-1} Raman shift interval, where a broad curvature was observed instead of a significant peak that sits on the Co_3O_4 and Cr_2O_3 locations. This section becomes more intense in specimen T8, suggesting that an increase in Cr concentration in the alloy would favor the formation of higher amounts of Cr_2O_3 in this section. Additionally, the peaks of MoO_3 around 660 cm^{-1} become more significant as the Co amount reduces, and the CoMoO_4 peak at about 920 cm^{-1} in TM-HT disappears. Hence, a reduction in Co concentration increases the presence of MoO_3 oxides in this section. However, it is worth noting that this banded section comprises fine patterns, and a slight shift in data collection location could result variations.

Figure 22 marks all distinguishable regions in the optical images of the wear surfaces of high-temperature POD tested specimens, and Raman data from these points are presented in Fig. 23. The color differences in optical images seem to be more informative about the oxide distribution on the surface than electron microscopy images. By the effect of heat treatment, it was shown that the matrix was splat in fine regions having higher accumulation Co, Mo, Si, and Cr (Fig. 5). Combining this transformation with a higher density of coatings obtained by smaller particle sizes, the overall structure becomes highly homogeneous in regards of these fine regions of increased concentration of certain elements. Consequently, coating density and heat treatment-driven diffusion and phase changes become effective in the distribution of the resultant oxidation products on the surface. Both favor a finer, highly blended, and homogeneous oxide structure on the surface. Furthermore, the initial alloy

Fig. 21 Raman analysis of oxide bands formed in room temperature tests of T4-HT, TM-HT and T8-HT specimens with points of analysis in attached images

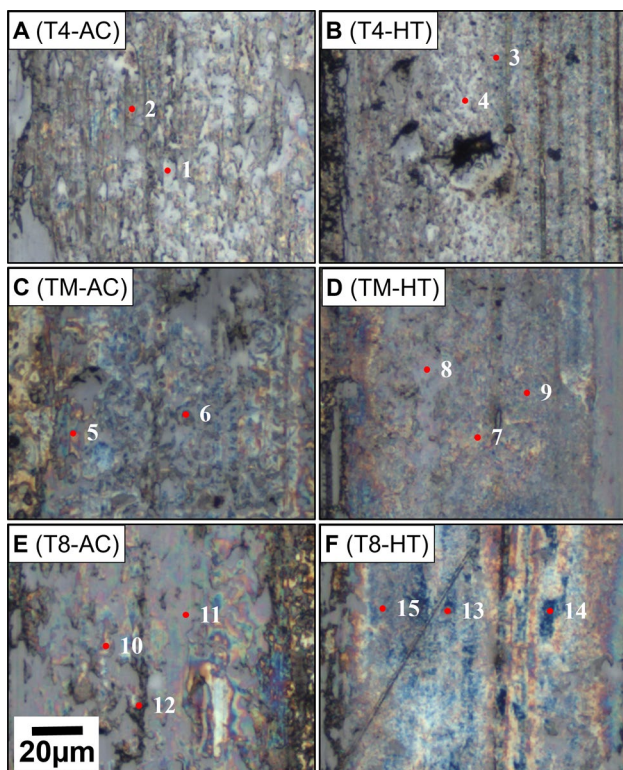
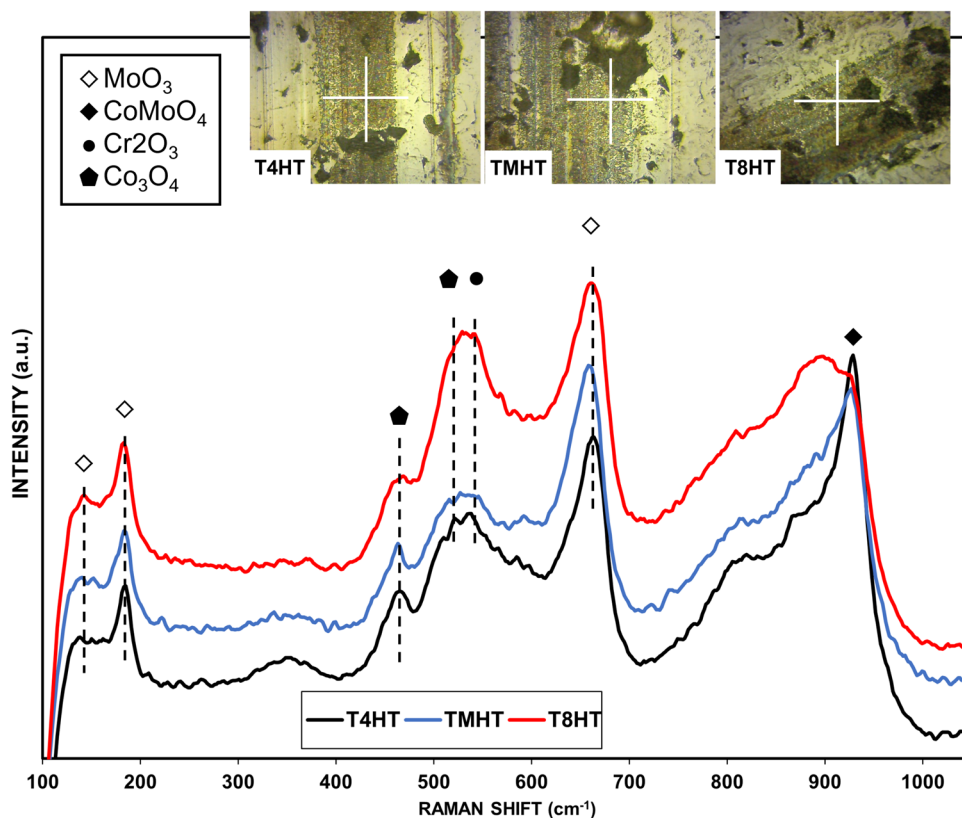


Fig. 22 Optical images of the wear tracks of 600 °C POD tested specimens marked for Raman surveys

composition introduces a higher degree of colorization to the surface which is best represented by Fig. 22F.

Upon inspection, traces of MoO_3 and Co_3O_4 were found on point 1 of specimen T4-AC, while point 2 showed the presence of CoMoO_4 (Fig. 23A). Point 1 exhibited a higher concentration of oxygen, and when comparing the surface area of phases represented by these points using Fig. 22, it was evident that a stronger Co_3O_4 and MoO_3 combination covered the surface of the specimen. After undergoing heat treatment, a more homogeneous distribution of oxide combination of Co and Mo oxides was observed in points 3 and 4 (Fig. 23B). Although a slight increase was noticed around 300 cm^{-1} at point 4, a suitable location for Cr_2O_3 , no significant peak was observed, making it impossible to detect any evidence of Cr_2O_3 on specimen T4 with its lowest Cr concentration. On the other hand, definitive peaks of Cr_2O_3 were found on points 5, 8, and 9 of specimen TM (Fig. 23C, D). Co and Mo oxides are still present, including Cr_2O_3 . Images of TM-AC and TM-HT in Fig. 22 indicated that Cr_2O_3 only partially covers the surface in its as-sprayed condition, but after heat treatment, although its formation was partial, it showed a better distribution on the surface with a finer structure. In specimen T8, Cr_2O_3 exhibited a significant presence in Raman shifts at every location in Fig. 23E, F. Within the scope of this investigation, it has been determined that the structures with blue tones observed in optical images in Fig. 22 are Cr_2O_3 and when the three alloys are compared,

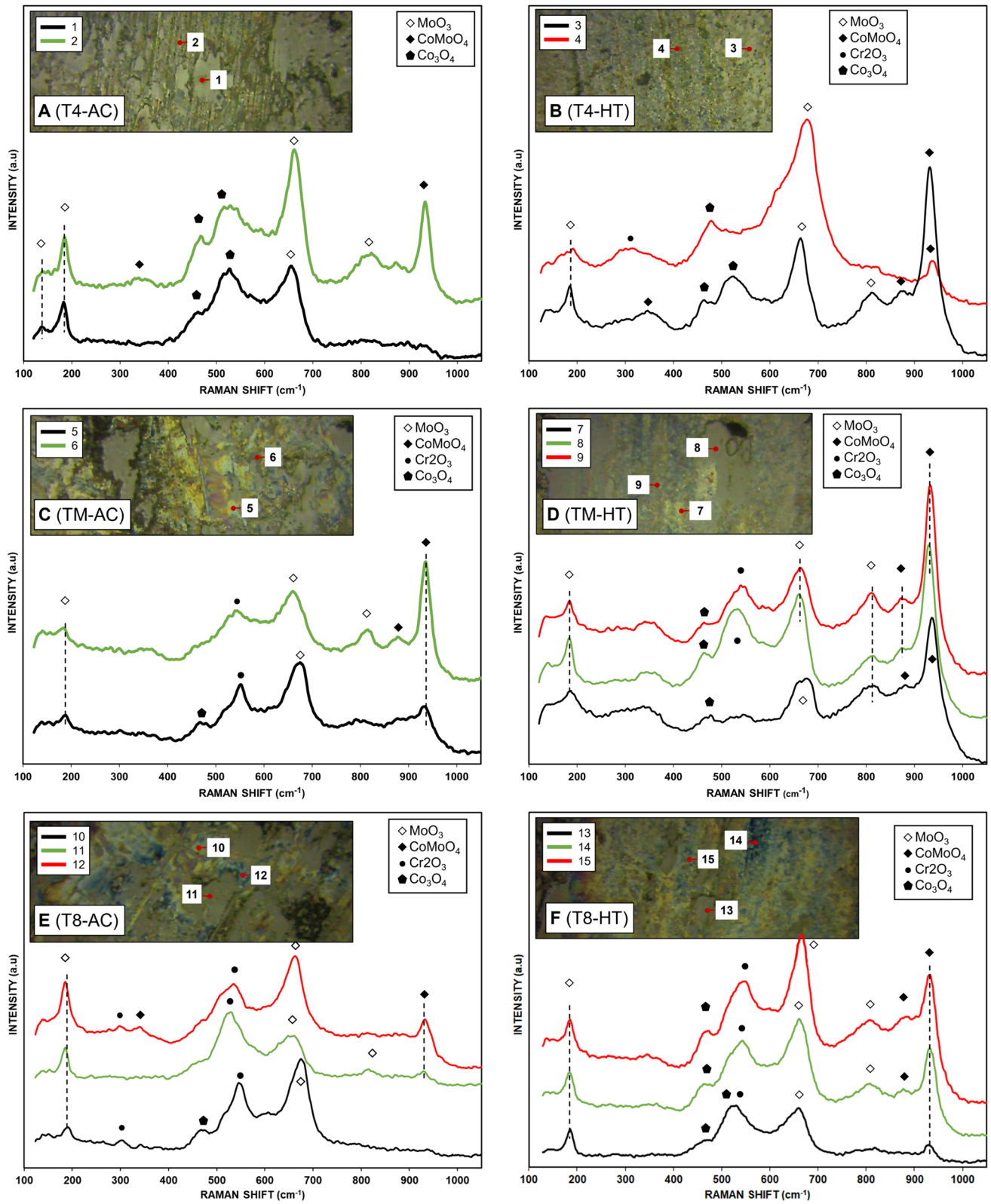


Fig. 23 Raman analysis of wear scars of all types of specimens tested at 600 °C

we can observe that the blue tones increase in proportion to the amount of Cr in the alloy content parallel to the findings of Raman studies.

The results presented in Figs. 24 and 25 demonstrate respectively the friction behaviors and wear rates of all specimens. Considering the friction coefficients, under the same heat treatment and testing conditions, all three alloys produce similar results.

As-sprayed specimens show a dramatic difference of wear rates which was expected upon initial inspection of Figs. 15A and 16. As previously noted [68], sliding wear generates dynamic loading conditions for materials, leading to the concept of fatigue crack propagation in the presence of discontinuities. Under these conditions, already present non-bonded boundaries act as cracks, and furthermore weak splat boundaries have higher possibility to turn into cracks and both of them act as stress concentrators. The overall density of both becomes the dominant factor over the overall performance of the coating under wear conditions. In micro-scratch tests, the density of splat boundaries was found to increase the number of cracks by a factor of at most 1.3, between specimens T4-AC and T8-AC. But with the dynamic loading conditions of wear tests, wear rate shows and increase of almost 3 and 5 folds respectively between T4-AC–TM-AC and TM-AC–T8-AC. In these testing conditions, it is difficult to distinguish the effect of hardness or alloy concentration from the effect of splat boundaries on the wear rates of the different specimens. Increased hardness with a higher number of crack-like boundaries would also

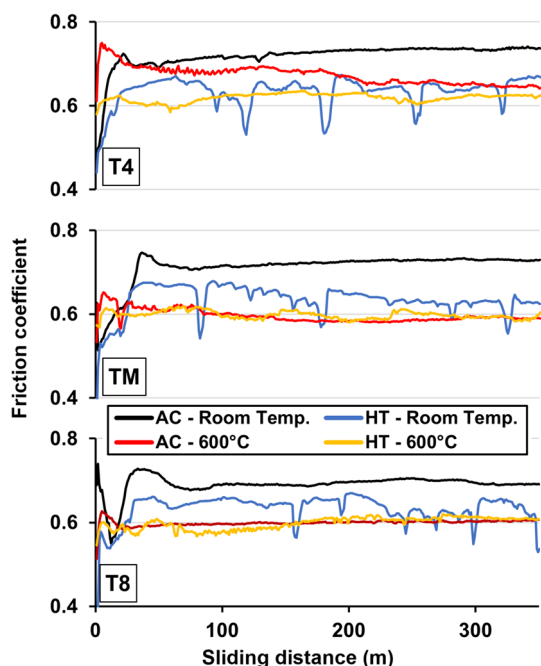


Fig. 24 Friction coefficient vs. sliding distance charts of POD tests at room temperature and 600 °C of all specimens

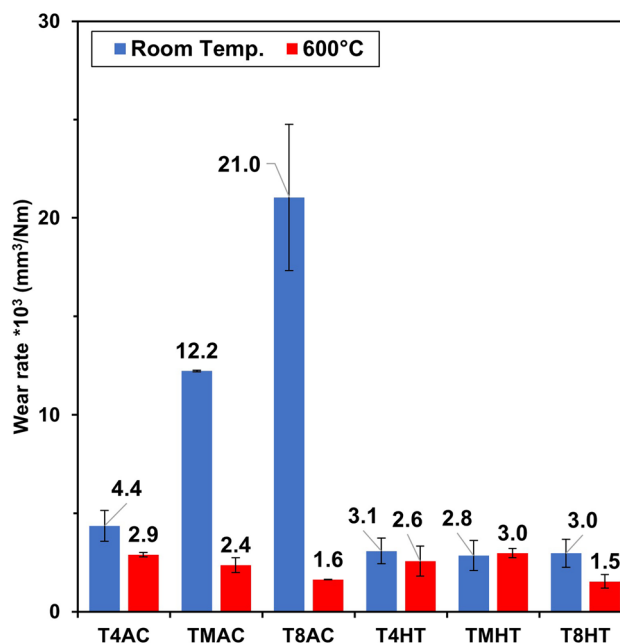


Fig. 25 Wear rates of POD tests at room temperature and 600 °C of all specimens

result in higher wear rates. However, the findings obtained in scratch tests and wear track morphologies suggest that splat boundary strength becomes the dominant factor against wear in room temperature tests of as-sprayed specimens.

Even with this great difference in wear rates it is interesting to note that as-sprayed specimens show similar friction behavior during room temperature wear conditions. These specimens take 50–100 m to reach a stable value, after which they exhibit a smooth and stable friction coefficient for the rest of the test. The specimen with the highest wear rate exhibits the greatest degree of oxidation, as explained by the mechanisms mentioned earlier (Fig. 15). Despite the noticeable surface degradation, the presence of oxidation and Co_7Mo_6 particles prevent any increase in the coefficient of friction. Additionally, since the scratch test results revealed no discernible difference in bonding strength between the three specimens, even as wear progresses, the underlying layers do not offer greater resistance to the pin than the initial degree.

The most interesting friction behavior was observed in room temperature tests of annealed specimens (Fig. 24). Experimental results indicate that these exhibit lower friction coefficients as compared to the as-sprayed specimens however, unlike the rest, the annealed specimens display certain irregularities along the test. At various locations some reverse peaks which may result a local reduction of 1.2 observable. Even though these seem sharp, it takes an average of 10 m for these peaks to form. Moreover, in some sections, like 100–200-m interval of TM-HT, a gradual

decrease with some frequent fluctuations is observable. After this section is completed, the coefficient shows a relatively rapid increase, reaching the values before this section. During the partial oxidation of the surface and the sections numbered 6 in Fig. 17, the friction coefficient decreases. As previously explained, with progress of wear, as these particles get detached or partially broken (Fig. 18), the pin starts to travel on a fresh constituent of the surface and friction coefficient increases again. This phenomenon has been previously studied and detailed by Bolelli et al. [27] but in our case the high durability and density and larger sizes of these particles exaggerate the effect of this event on friction coefficient.

Even with all these fluctuations in friction coefficients, after annealing, all three specimens show very close wear rates around $3 \times 10^{-3} \text{ mm}^3/\text{Nm}$ (Fig. 25). Parallel to the cracking behavior, especially to the final sections of micro-scratch testing, splat boundary cohesion after annealing both decreases the wear rates and at the same time neutralizes the effect of the density of the splat boundaries on the wear performance. Even though there are significant hardness differences among the specimens after annealing, similar wear rate results also support the above-mentioned dominance of the splat boundary strength on the wear rates.

At elevated temperatures oxide films covering the surface of the specimens increase the overall friction performance under sliding conditions (Fig. 24). Except for specimen T4, specimens TM and T8 show a mean and smooth friction coefficient of around 0.6 for both AC and HT conditions. Unlike these two specimens, T4 shows slightly increased values of friction coefficient both in AC and HT conditions. As already covered above, the main difference between specimen T4 and the other two is the coarser surface pattern of oxide concentration in both conditions and the absence of Cr_2O_3 on the surface. These two properties provide weaker oxide protection than the other specimens and result in higher degrees of friction. For T4-AC we see a gradual decrease during the test which suggests that oxidation takes place at a slower degree again compared to the other specimens. In this aspect formation of Cr_2O_3 and MoO_3 gains importance. With the presence of higher amounts of Cr and relatively higher amounts of Mo with respect to Co in their structure both TM and T8 can generate functional oxide films at the earlier stages of the tests and achieve lower friction during the tests. When T4-HT is compared with T4-AC, even with the same alloy composition, homogeneous oxidation of the surface provides a better protection against friction, but still, its friction remains higher than TM and T8.

Parallel to the friction behavior, wear rates at elevated temperature tests show the importance of oxide films covering the surface. At 600 °C, this time except T8, all specimens reveal a wear rate between about $2.5\text{--}3.0 \times 10^{-3} \text{ mm}^3/\text{Nm}$ (Fig. 25) which are very close to annealed specimens.

T8 shows further decrease, reaching values of $1.5 \times 10^{-3} \text{ mm}^3/\text{Nm}$. Comparison of T4 and TM shows that if the surface integrity is high, the wear loss can be low even with the higher rates of friction under the selected testing condition. Considering the wear behavior of the T8, the aforementioned change in Co and Mo-based oxide distribution and the formation of Cr_2O_3 on the entire surface results in a wear loss of half of the other samples. Consequently, at elevated temperatures like 600 °C, surface oxidation becomes superior to splat boundary strength. It both increases the surface integrity and with the lubricating properties, decreases the friction coefficient. In this aspect alloy composition becomes the most important factor determining the resultant oxidation products and hence the performance of the alloy at high temperatures.

4 Conclusion

This study examined the impact of powder particle size, three different alloy composition, and annealing heat treatment at 900 °C, and how these factors affect microstructure, mechanical properties, and wear performance. After thorough investigation, it was found that:

1. The High Velocity Oxygen Fuel (HVOF) process yields a predominantly amorphous coating owing to its incredibly high cooling rates. The amorphous coating is indicative of the complete melting of initially crystalline powders.
2. After undergoing annealing heat treatment for four hours at 900 °C, all alloy compositions displayed significant crystallization in their structures and solid-state diffusion bonding across the splat boundaries. The resultant structure comprises a Co-based solid solution, which is embedded with hard Laves.
3. The increase of Cr in the Co matrix results in a gradual enhancement of hardness, attributed to the formation of Mo-based Laves phases at a higher degree. This phenomenon is also observable in as-sprayed conditions but becomes more pronounced after annealing.
4. A decrease in powder particle size leads to the formation of a finer and denser structure resulting in the augmentation of the splat boundary density.
5. In as-coated condition, splat boundary strength is the most essential property of the coating that exerts a direct influence on the mechanical performance. As per the chosen spray parameters, it has been observed that the strength of the boundaries is not significantly influenced by the alloy composition or particle size. However, an increase in boundary density, coupled with higher hardness, leads to a heightened susceptibility to fractures.

- under external forces, ultimately resulting in a decline in the coating's overall performance.
6. Annealing for 4 h at 900 °C increases splat bonding strength about four times, increases the toughness, and dramatically decreases cracking behavior against loads. In contrast to specimens in their as-sprayed condition, an increase in Cr concentration promotes the formation of the higher volume of CrSi₂ particles in the neighborhood to the splat boundaries, promoting the curing of a greater volume of splat boundaries.
 7. The properties mentioned in points 5 and 6 also provide the general framework for the wear behavior. However, under the dynamic loading conditions of wear, the negative influence of the boundaries and brittleness over structural integrity increases, resulting in higher degrees of wear in as-sprayed coatings. On the other hand, annealing strengthened coating shows significantly increased yet similar wear performance for all three alloys.
 8. At 600 °C, the surface oxide layer exhibits a dominant influence on wear characteristics. Specifically, the composition and distribution of oxides have been identified as the most effective protective mechanism against wear, which overcomes the inherent drawbacks associated with the splat boundaries and brittleness of the structure. Additionally, surface oxide layers serve to maintain structural integrity and reduce friction during wear. The incorporation of higher concentrations of Cr and Mo into the alloy promotes the formation of a wide variety of oxides, thereby ensuring better protection against wear.

In essence, the integrity and mechanical behavior of a structure heavily rely on its splat boundaries. These boundaries serve as the foundation of the coating's strength. In as-sprayed condition the bonding strength in between splats may be very low and the boundaries may act as vulnerable locations against forces. However, when subjected to annealing heat treatment, with solid-state diffusion phenomenon bonding strength can be increased significantly. Furthermore, at elevated temperatures, the formation of an oxide layer on the surface serves as a protective layer for the coating. Hence, even with high density of splat boundaries, the coatings can be trusted at elevated temperatures. However, care should be taken that under increased forces, the surface oxide layer may also remain weak to maintain the integrity of the coating. Therefore, it is imperative to thoroughly analyze the thickness and strength of the oxide layer under operating temperatures and conditions. Additionally, extended use of the coating at elevated temperatures can enhance splat cohesion and overall performance. Employing the coatings in high-temperature environments can create ideal conditions that help prevent any potential weaknesses.

Author Contributions We confirm that the manuscript has been read and approved by all named authors and that there are no other persons who satisfied the criteria for authorship but are not listed. We further confirm that the order of authors listed in the manuscript has been approved by all of us. We confirm that we have given due consideration to the protection of intellectual property associated with this work and that there are no impediments to publication, including the timing of publication, with respect to intellectual property. In so doing we confirm that we have followed the regulations of our institutions concerning intellectual property. We understand that the Corresponding Author is the sole contact for the Editorial process (including Editorial Manager and direct communications with the office). He is responsible for communicating with the other authors about progress, submissions of revisions and final approval of proofs. We confirm that we have provided a current, correct email address which is accessible by the Corresponding Author.

Funding Open access funding provided by the Scientific and Technological Research Council of Türkiye (TÜBİTAK).

Declarations

Conflict of interest We wish to confirm that there are no known conflicts of interest associated with this publication and there has been no significant financial support for this work that could have influenced its outcome.

Open Access This article is licensed under a Creative Commons Attribution 4.0 International License, which permits use, sharing, adaptation, distribution and reproduction in any medium or format, as long as you give appropriate credit to the original author(s) and the source, provide a link to the Creative Commons licence, and indicate if changes were made. The images or other third party material in this article are included in the article's Creative Commons licence, unless indicated otherwise in a credit line to the material. If material is not included in the article's Creative Commons licence and your intended use is not permitted by statutory regulation or exceeds the permitted use, you will need to obtain permission directly from the copyright holder. To view a copy of this licence, visit <http://creativecommons.org/licenses/by/4.0/>.

References

1. P.M. Natishan, S.H. Lawrence, R.L. Foster, J. Lewis, B.D. Sartwell, Salt fog corrosion behavior of high-velocity oxygen-fuel thermal spray coatings compared to electrodeposited hard chromium. *Surf. Coat. Technol.* **130**, 218–223 (2000). [https://doi.org/10.1016/S0257-8972\(00\)00671-X](https://doi.org/10.1016/S0257-8972(00)00671-X)
2. B.D. Sartwell, P.M. Natishan, I.L. Singer, K.O. Legg, J.D. Schell, J.P. Sauer, Replacement of Chromium Electroplating Using HVOF Thermal Spray Coatings, Paper presented at the 34th Aerospace/Airline Plating & Metal Finishing Forum, San Antonio, Texas, 1998
3. C.D. Prasad, S. Joladarashi, M.R. Ramesh, M.S. Srinath, B.H. Channabasappa, Influence of microwave hybrid heating on the sliding wear behaviour of HVOF sprayed CoMoCrSi coating. *Mater. Res. Express* **5**, 86519 (2018). <https://doi.org/10.1088/2053-1591/aad44e>
4. T. Sahraoui, H.I. Feraoun, N. Fenineche, G. Montavon, H. Aourag, C. Coddet, HVOF-sprayed Tribaloy®-400: microstructure and first principle calculations. *Mater. Lett.* **58**, 2433–2436 (2004). <https://doi.org/10.1016/j.matlet.2004.02.025>

5. J.R. Davis, Thermal Spray Society Training Committee, *Handbook of Thermal Spray Technology* (ASM International, Almere, 2004)
6. A.P. Buang, R. Liu, X.J. Wu, M.X. Yao, Cracking analysis of HVOF coatings under Vickers indentation. *J. Coat. Technol. Res.* **5**, 513–534 (2008). <https://doi.org/10.1007/s11998-008-9106-8>
7. J.Y. Cho, S.H. Zhang, T.Y. Cho, J.H. Yoon, Y.K. Joo, S.K. Hur, The processing optimization and property evaluations of HVOF Co-base alloy T800 coating. *J. Mater. Sci.* **44**, 6348–6355 (2009). <https://doi.org/10.1007/s10853-009-3875-z>
8. C.D. Prasad, S. Joladarashi, M.R. Ramesh, M.S. Srinath, B.H. Channabasappa, Development and sliding wear behavior of Co–Mo–Cr–Si cladding through microwave heating. *Silicon* **11**, 2975–2986 (2019). <https://doi.org/10.1007/s12633-019-0084-5>
9. B. Wielage, A. Wank, H. Pokhmurska, T. Grund, C. Rupprecht, G. Reisel, E. Friesen, Development and trends in HVOF spraying technology. *Surf. Coat. Technol.* **201**, 2032–2037 (2006). <https://doi.org/10.1016/j.surfcoat.2006.04.049>
10. T. Sahraoui, N.E. Fenineche, G. Montavon, C. Coddet, Alternative to chromium: characteristics and wear behavior of HVOF coatings for gas turbine shafts repair (heavy-duty). *J. Mater. Process. Technol.* **152**, 43–55 (2004). <https://doi.org/10.1016/j.jmatprotec.2004.02.061>
11. G. Bolelli, L. Lusvarghi, F. Pighetti Mantini, M. Barletta, F. Casadei, Microstructural and tribological characterisation of as sprayed and heat treated HVOF deposited Ni alloys. *Surf. Eng.* **23**, 355–372 (2007). <https://doi.org/10.1179/174329407X247172>
12. A. Rehman, Y. Liang, M. Hassan Shirani Bidabadi, Z. Yu, C. Zhang, H. Chen, Z.G. Yang, Enhancement of cyclic oxidation resistance and effect of transition oxides on wear mechanism of yttrium plus aluminium modified tribaloy T-900 alloy. *Corros. Sci.* **163**, 10828 (2020). <https://doi.org/10.1016/j.corsci.2019.108283>
13. T. Durejko, M. Łazińska, J. Dworecka-Wójcik, S. Lipiński, R.A. Varin, T. Czujko, The Tribaloy T-800 coatings deposited by laser engineered net shaping (LENS™). *Materials* **12**, 1366 (2019). <https://doi.org/10.3390/ma12091366>
14. R.G. Bohatch, K. Graf, A. Scheid, Effect of track overlap on the microstructure and properties of the CoCrMoSi PTA coatings. *Mater. Res.* **18**, 553–562 (2015). <https://doi.org/10.1590/1516-1439.340014>
15. Z. Yudu, Y. Zhigang, Z. Chi, L. Hao, Effect of rhenium addition on isothermal oxidation behavior of Tribaloy T-800 alloy. *Chin. J. Aeronaut.* **23**, 370–376 (2010). [https://doi.org/10.1016/S1000-9361\(09\)60229-6](https://doi.org/10.1016/S1000-9361(09)60229-6)
16. C. Navas, M. Cadenas, J.M. Cuetos, J. de Damborenea, Microstructure and sliding wear behaviour of Tribaloy T-800 coatings deposited by laser cladding. *Wear* **260**, 838–846 (2006). <https://doi.org/10.1016/j.wear.2005.04.020>
17. F. Parreiras Marques, A. César Bozzi, C. Scandian, A. Paulo Tschiptschin, Microabrasion of three experimental cobalt-chromium alloys: wear rates and wear mechanisms. *Wear* **390–391**, 176–183 (2017). <https://doi.org/10.1016/j.wear.2017.07.023>
18. R. Liu, J. Yao, Q. Zhang, M.X. Yao, R. Collier, Effects of silicon content on the microstructure and mechanical properties of cobalt-based Tribaloy alloys. *J. Eng. Mater. Technol.* **138**, 041017 (2016). <https://doi.org/10.1115/1.4034075>
19. J.H. Zhu, C.T. Liu, L.M. Pike, P.K. Liaw, Thermodynamic interpretation of the size-ratio limits for Laves phase formation. *Metall. Mater. Trans. A Phys. Metall. Mater. Sci.* **30**, 1449–1452 (1999). <https://doi.org/10.1007/s11661-999-0292-5>
20. X.H. Zhang, C. Zhang, Y.D. Zhang, S. Salam, H.F. Wang, Z.G. Yang, Effect of yttrium and aluminum additions on isothermal oxidation behavior of Tribaloy T-700 alloys. *Corros. Sci.* **88**, 405–415 (2014). <https://doi.org/10.1016/j.corsci.2014.07.053>
21. M.X. Yao, J.B.C. Wu, S. Yick, Y. Xie, R. Liu, High temperature wear and corrosion resistance of a laves phase strengthened Co–Mo–Cr–Si alloy. *Mater. Sci. Eng. A* **435–436**, 78–83 (2006). <https://doi.org/10.1016/j.msea.2006.07.054>
22. A. Sharma, F. Sadeghi, A. Sharma, Experimental investigation of fretting wear of coated spring clip and inlet ring in land-based gas turbines at elevated temperature. *Wear* **446–447**, 203200 (2020). <https://doi.org/10.1016/j.wear.2020.203200>
23. A. Rehman, Y. Liang, M.H.S. Bidabadi, Z. Yu, C. Zhang, H. Chen, Z. Yang, gang: comparative cyclic oxidation behaviour and effect of oxides on hardness of wear resistance coating alloys T-401 and T-900. *J. Iron. Steel Res. Int.* **26**, 1069–1079 (2019). <https://doi.org/10.1007/s42243-019-00258-2>
24. R. Liu, M.X. Yao, P.C. Patnaik, X. Wu, Effects of heat treatment on mechanical and tribological properties of cobalt-base Tribaloy alloys. *J. Mater. Eng. Perform.* **14**, 634–640 (2005). <https://doi.org/10.1361/105994905X64567>
25. A. Halstead, R.D. Rawlings, The fracture behaviour of two Co–Mo–Cr–Si wear resistant alloys (“Triballoys”). *J. Mater. Sci.* **20**, 1248–1256 (1985). <https://doi.org/10.1007/BF01026320>
26. G. Bolelli, L. Lusvarghi, Tribological properties of HVOF as-sprayed and heat treated Co–Mo–Cr–Si coatings. *Tribol. Lett.* **25**, 43–54 (2007). <https://doi.org/10.1007/s11249-006-9136-2>
27. G. Bolelli, L. Lusvarghi, Heat treatment effects on the tribological performance of HVOF sprayed Co–Mo–Cr–Si coatings. *Proc. Int. Therm. Spray Conf.* **15**, 802–810 (2006). <https://doi.org/10.1361/105996306X146721>
28. H. Guo, X. Zhao, Y. An, H. Zhou, P. Yan, Z. Wu, J. Chen, Fabrication and effect of heat treatment on the microstructure and tribology properties of HVOF-sprayed CoMoCrSi coating. *J. Mater. Sci.* **56**, 12423–12437 (2021). <https://doi.org/10.1007/s10853-021-05986-z>
29. H. Guo, B. Li, P. Yan, Z. Wu, Microstructures, mechanical properties and tribological behaviors of HVOF-sprayed CoMoCrSi alloy coatings before and after 800 °C-annealed treatment. *J. Alloys Compd.* **909**, 164662 (2022). <https://doi.org/10.1016/j.jallcom.2022.164662>
30. L. Tang, P. He, J. Kang, L. Wang, S. Ding, S. Chen, X. Zhu, F. Xie, L. Zhou, G. Ma, H. Wang, Significantly enhanced mechanical and tribological properties of Co-based alloy coatings by annealing treatment. *Tribol. Int.* **146**, 106265 (2020). <https://doi.org/10.1016/j.triboint.2020.106265>
31. Y. Wang, J. Liu, N. Kang, G. Darut, T. Poirier, J. Stella, H. Liao, M.P. Planche, Cavitation erosion of plasma-sprayed CoMoCrSi coatings. *Tribol. Int.* **102**, 429–435 (2016). <https://doi.org/10.1016/j.triboint.2016.06.014>
32. W.J. Yang, L. Zou, X.Y. Cao, J.H. Liu, D.J. Li, Z.B. Cai, Fretting wear properties of HVOF-sprayed CoMoCrSi coatings with different spraying parameters. *Surf. Coat. Technol.* **358**, 994–1005 (2019). <https://doi.org/10.1016/j.surfcoat.2018.12.039>
33. J. Sha, L.Y. Chen, Y.T. Liu, Z.J. Yao, S. Lu, Z.X. Wang, Q.H. Zang, S.H. Mao, L.C. Zhang, Phase transformation-induced improvement in hardness and high-temperature wear resistance of plasma-sprayed and remelted NiCrBSi/WC coatings. *Metals* **10**, 1688 (2020). <https://doi.org/10.3390/met10121688>
34. H.N. Xuan, L.Y. Chen, N. Li, H. Wang, C. Zhao, M. Bobrov, S. Lu, L.C. Zhang, Temperature profile, microstructural evolution, and wear resistance of plasma-sprayed NiCrBSi coatings under different powers in a vertical remelting way. *Mater. Chem. Phys.* **292**, 126773 (2022). <https://doi.org/10.1016/j.matchemphys.2022.126773>
35. L.Y. Chen, T. Xu, S. Lu, Z.X. Wang, S. Chen, L.C. Zhang, Improved hardness and wear resistance of plasma sprayed nano-structured NiCrBSi coating via short-time heat treatment. *Surf.*

- Coat. Technol. **350**, 436–444 (2018). <https://doi.org/10.1016/j.surfcoat.2018.07.037>
36. H.N. Xuan, N. Li, J. Zhang, T. Xu, L. Zhang, J. Cheng, D. Oleksandr, S. Lu, L.Y. Chen, Different primary gas flow rates in determining the flattening behavior of in-flight particles in plasma-sprayed NiCrBSi coatings and the resultant microstructure and hardness. *Metals* **13**, 1966 (2023). <https://doi.org/10.3390/met13121966>
 37. N.M. Chavan, B. Kiran, A. Jyothirmayi, P.S. Phani, G. Sundararajan, The corrosion behavior of cold sprayed zinc coatings on mild steel substrate. *J. Therm. Spray Technol.* **22**, 463–470 (2013). <https://doi.org/10.1007/s11666-013-9893-z>
 38. S. Alidokht, Y. Gao, B.C.N.M. de Castilho, N. Sharifi, M. Harfouche, P. Stoyanov, M. Makowiec, C. Moreau, R.R. Chromik, Microstructure and mechanical properties of Tribaloy coatings deposited by high-velocity oxygen fuel. *J. Mater. Sci.* **57**, 20056–20068 (2022). <https://doi.org/10.1007/s10853-022-07843-z>
 39. K.P. Gupta, The Co–Cr–Si (cobalt–chromium–silicon) system. *J. Phase Equilibria Diffus.* **31**, 300–307 (2010). <https://doi.org/10.1007/s11669-010-9670-3>
 40. A.A. Aleksandrov, V.Y. Dashevskii, B.V. Linchevskii, Thermodynamics of the oxygen solutions in chromium-containing melts of the Fe–Co system. *Russ. Metall. (Metally)*. **2014**, 681–687 (2014). <https://doi.org/10.1134/S003602951409002X>
 41. X. Wu, R. Liu, X. Zhang, M.X. Yao, Microstructure and wear performance of high-entropy triballoy alloys. *J. Mater. Eng. Perform.* (2023). <https://doi.org/10.1007/s11665-023-08349-8>
 42. Š Houdková, E. Smazalová, M. Vostřák, J. Schubert, Properties of NiCrBSi coating, as sprayed and remelted by different technologies. *Surf. Coat. Technol.* **253**, 14–26 (2014). <https://doi.org/10.1016/j.surfcoat.2014.05.009>
 43. W.-Y. Li, C.-J. Li, H. Liao, Effect of annealing treatment on the microstructure and properties of cold-sprayed Cu coating. *J. Therm. Spray Technol.* **15**, 206–211 (2006). <https://doi.org/10.1361/105996306X108066>
 44. G. Sundararajan, N.M. Chavan, S. Kumar, The elastic modulus of cold spray coatings: influence of inter-splat boundary cracking. *J. Therm. Spray Technol.* **22**, 1348–1357 (2013). <https://doi.org/10.1007/s11666-013-0034-5>
 45. N.M. Chavan, M. Ramakrishna, P.S. Phani, D.S. Rao, G. Sundararajan, The influence of process parameters and heat treatment on the properties of cold sprayed silver coatings. *Surf. Coat. Technol.* **205**, 4798–4807 (2011). <https://doi.org/10.1016/j.surfcoat.2011.04.063>
 46. G. Sundararajan, N.M. Chavan, G. Sivakumar, P. Sudharshan Phani, Evaluation of parameters for assessment of inter-splat bond strength in cold-sprayed coatings. *J. Therm. Spray Technol.* **19**, 1255–1266 (2010). <https://doi.org/10.1007/s11666-010-9527-7>
 47. S. Jiang, U. Yin, I. Zhang, A. Zhao, H. Li, 800 °C isothermal section of the Co–Cr–Mo–Si quaternary system. *Int. J. Mater. Res.* **105**, 1191–1201 (2014). <https://doi.org/10.3139/146.111130>
 48. K.P. Gupta, The Co–Cr–Mo (cobalt–chromium–molybdenum) system. *J. Phase Equilibria Diffus.* **26**, 87–92 (2005). <https://doi.org/10.1361/15477030522608>
 49. H. Okamoto, Mo–Si (molybdenum–silicon). *J. Phase Equilibria Diffus.* **32**, 176 (2011). <https://doi.org/10.1007/s11669-010-9843-0>
 50. F. Stein, A. Leineweber, Laves phases: a review of their functional and structural applications and an improved fundamental understanding of stability and properties. *J. Mater. Sci.* **56**, 5321–5427 (2021). <https://doi.org/10.1007/s10853-020-05509-2>
 51. W. Xu, R. Liu, P.C. Patnaik, M.X. Yao, X.J. Wu, Mechanical and tribological properties of newly developed Triballoy alloys. *Mater. Sci. Eng. A* **452–453**, 427–436 (2007). <https://doi.org/10.1016/j.msea.2006.10.088>
 52. F. Chandoul, A. Boukhachem, F. Hosni, H. Moussa, M.S. Fayache, M. Amlouk, R. Schneider, Change of the properties of nanostructured MoO₃ thin films using gamma-ray irradiation. *Ceram. Int.* **44**, 12483–12490 (2018). <https://doi.org/10.1016/j.ceramint.2018.04.040>
 53. K.K. Wang, F.X. Wang, Y.D. Liu, G.B. Pan, Vapor growth and photoconductive property of single-crystalline MoO₃ nanosheets. *Mater. Lett.* **102–103**, 8–11 (2013). <https://doi.org/10.1016/j.matlet.2013.03.092>
 54. H. Sun, H. Zhang, X. Jing, J. Hu, K. Shen, Z. Liang, J. Hu, Q. Tian, M. Luo, Z. Zhu, Z. Jiang, H. Huang, F. Song, One-step synthesis of centimeter-size alpha-MoO₃ with single crystallinity. *Appl. Surf. Sci.* **476**, 789–795 (2019). <https://doi.org/10.1016/j.apsusc.2019.01.169>
 55. T. Yang, H. Zhang, Y. Luo, L. Mei, D. Guo, Q. Li, T. Wang, Enhanced electrochemical performance of CoMoO₄ nanorods/reduced graphene oxide as anode material for lithium-ion batteries. *Electrochim. Acta* **158**, 327–332 (2015). <https://doi.org/10.1016/j.electacta.2015.01.154>
 56. G. Jiang, L. Li, Z. Huang, Z. Xie, B. Cao, Rod-like porous CoMoO₄@C as excellent anode for high performance lithium ion battery. *J. Alloys Compd.* **790**, 891–899 (2019). <https://doi.org/10.1016/j.jallcom.2019.03.283>
 57. F. Nti, D.A. Anang, J.I. Han, Facilely synthesized NiMoO₄/CoMoO₄ nanorods as electrode material for high performance supercapacitor. *J. Alloys Compd.* **742**, 342–350 (2018). <https://doi.org/10.1016/j.jallcom.2018.01.289>
 58. V. Vinothkumar, M. Abinaya, S.M. Chen, Ultrasonic assisted preparation of CoMoO₄ nanoparticles modified electrochemical sensor for chloramphenicol determination. *J. Solid State Chem.* **302**, 122392 (2021). <https://doi.org/10.1016/j.jssc.2021.122392>
 59. X. Xu, J. Shen, N. Li, M. Ye, Microwave-assisted synthesis of graphene/CoMoO₄ nanocomposites with enhanced supercapacitor performance. *J. Alloys Compd.* **616**, 58–65 (2014). <https://doi.org/10.1016/j.jallcom.2014.07.047>
 60. V.G. Hadjiev, M.N. Iliev, I.V. Vergilov, The Raman spectra of Co₃O₄. *J Phys C*. **21**, L199–L201 (1988). <https://doi.org/10.1088/0022-3719/21/7/007>
 61. J. Olejníček, J. Šmíd, R. Perekrestov, P. Kšířová, J. Rathouský, M. Kohout, M. Dvořáková, Š Kment, K. Jurek, M. Čada, Z. Hubička, Co₃O₄ thin films prepared by hollow cathode discharge. *Surf. Coat. Technol.* **366**, 303–310 (2019). <https://doi.org/10.1016/j.surfcoat.2019.03.010>
 62. B. Rivas-Murias, V. Salgueiriño, Thermodynamic CoO–Co₃O₄ crossover using Raman spectroscopy in magnetic octahedron-shaped nanocrystals. *J. Raman Spectrosc.* **48**, 837–841 (2017). <https://doi.org/10.1002/jrs.5129>
 63. Y. Liu, X. Zhang, Y. Wu, Electrochemical behavior of Co₃O₄ microspheres in aqueous LiOH solution. *Rare Met.* **30**, 90–93 (2011). <https://doi.org/10.1007/s12598-011-0245-1>
 64. I. Lorite, J.J. Romero, J.F. Fernández, Effects of the agglomeration state on the Raman properties of Cr₂O₃ nanoparticles. *J. Raman Spectrosc.* **43**, 1443–1448 (2012). <https://doi.org/10.1002/jrs.4098>
 65. M. Roy, S. Ghosh, M.K. Naskar, Solvothermal synthesis of Cr₂O₃ nanocubes via template-free route. *Mater. Chem. Phys.* **159**, 101–106 (2015). <https://doi.org/10.1016/j.matchemphys.2015.03.058>
 66. J. Singh, V. Verma, R. Kumar, Preparation and structural, optical studies of Al substituted chromium oxide (Cr₂O₃) nanoparticles. *Vacuum* **159**, 282–286 (2019). <https://doi.org/10.1016/j.vacuum.2018.09.033>
 67. S.I. Dolgaev, N.A. Kirichenko, G.A. Shafeev, Deposition of nanostructured Cr₂O₃ on amorphous substrates under laser irradiation of the solid–liquid interface. *Appl. Surf. Sci.* **138–139**, 449–454 (2019). [https://doi.org/10.1016/S0169-4332\(98\)00439-5](https://doi.org/10.1016/S0169-4332(98)00439-5)
 68. H. Guo, Y. Wang, E. Hao, B. Li, Y. An, J. Chen, H. Zhou, P. Yan, Z. Wu, CoMoCrSi coatings prepared by high-velocity oxygen fuel

spraying: microstructure and mechanical properties at elevated temperatures up to 800 °C. *Mater. Res. Express* **6**, 1265e9 (2019).
<https://doi.org/10.1088/2053-1591/ab6374>

Publisher's Note Springer Nature remains neutral with regard to jurisdictional claims in published maps and institutional affiliations.